KfK 3508
Dezember 1983

Temperature Escalation in PWR Fuel Rod Simulator Bundles due to the Zircaloy/Steam Reaction
Test ESBU-1
Test Results Report

S. Hagen, H. Malauschek, S. O. Peck, K. P. Wallenfels
Hauptabteilung Ingenieurtechnik

Kernforschungszentrum Karlsruhe

KERNFORSCHUNGSZENTRUM KARLSRUHE
HAUPTABTEILUNG INGENIEURTECHNIK
PROJEKT NUKLEARE SICHERHEIT

KfK 3508

Temperature Escalation in PWR Fuel Rod Simulator Bundles due to the Zircaloy/Steam Reaction:
Test ESBU-1
Test Results Report

S. Hagen, H. Malauschek, S.O. Peck+), K.P. Wallenfels

+) USNRC Delegate to Kernforschungszentrum Karlsruhe from EG&G, Idaho Falls, Idaho.

KERNFORSCHUNGSZENTRUM KARLSRUHE GMBH, KARLSRUHE

Kernforschungszentrum Karlsruhe GmbH
ISSN 0303-4003

Summary

This report describes the test conduct and results of the bundle test ESBU-1. The test objective was the investigation of temperature escalation of zircaloy clad fuel rods. The investigation of the temperature escalation is part of a program of out-of-pile experiments, performed within the framework of the PNS Severe Fuel Damage Program.

The bundle was composed of a 3x3 array of fuel rod simulators surrounded by a zircaloy shroud which was insulated with a ZrO_2 fiber ceramic wrap. The fuel rod simulators comprised a tungsten heater, UO_2 annular pellets, and zircaloy cladding over a 0.4 m heated length. A steam flow of 1 g/s was inlet to the bundle.

The most pronounced temperature escalation was found on the central rod. The initial heatup rate of 2°C/s at 1100°C increased to approximately 6°C/s. The maximum temperature reached was 2250°C. The following fast temperature decrease was caused by runoff of molten zircaloy.

Molten zircaloy swept down the thin cladding oxide layer formed during heatup. The melt dissolved the surface of the UO_2 pellets and refroze as a coherent lump in the lower part of the bundle. The remaining pellets fragmented during cooldown and formed a powdery layer on the refrozen lump. The lump was sectioned posttest at several elevations: Dissolution of UO_2 by the molten zircaloy, interaction between the melt and previously oxidized zircaloy, and oxidation of the melt had occurred.

Temperatureskalation infolge der Zirkaloy/Wasserdampf-Reaktion an Bündeln aus Druckwasserreaktor-Brennstabsimulatoren: Versuchsergebnisse Test ESBU-1.

Kurzfassung

Dieser KfK-Bericht beschreibt die Versuchsdurchführung und die Ergebnisse des Bündelexperiments ESBU-1 für die Untersuchung der Temperatureskalation von zirkaloyumhüllten Brennelementstaben. Die Untersuchung des Eskalationsverhaltens gehört zum Programm der Out-of-pile Experimente, die im Rahmen der Severe Fuel Damage Untersuchungen des PNS durchgeführt werden.

Das Bündel war in einer 3x3 Anordnung aus unseren üblichen Brennstabsimulatoren aufgebaut. Die Brennstabsimulatoren bestanden aus dem zentralen Heizer, den UO_2-Ringpellets und dem Zirkaloy-Hüllrohr. Das Bündel war von einem Zirkaloy-Vierkantrohr und 6 mm ZrO_2 Faser-Isolation umgeben. Die Länge betrug 40 cm. Der Dampffluß durch das Bündel betrug 1g/s.

Die ausgepragteste Temperatureskalation trat am Zentralstab auf. Der Temperaturanstieg von 2°C/s bei 1100°C nahm auf 6°C/s zu. Die maximal erreichte Temperatur lag bei ca. 2250°C. Die anschließende schnelle Temperaturabnahme wurde durch das Ablaufen des geschmolzenen Zirkaloys aus dem Reaktionsbereich bedingt. Das geschmolzene Zirkaloy hat die nur dünne Oxidschicht der Hülle mit heruntergespült und ist dann zu einem zusammenhängenden Klumpen erstarrt. Während seiner Kontaktzeit mit den Pellets hat das flüssige Zirkaloy einen deutlichen Teil des Ringpellets gelöst. Beim Abkühlen ist der Rest des Pellets verbröselt und hat eine puderförmige Schüttung auf dem Schmelzklumpen gebildet. Die am Schmelzklumpen durchgeführten Schnitte zeigen die Blockierung des Bündelquerschnitts mit der Ausnahme eines einzigen Kanals. Die Wechselwirkung der Schmelze mit den oxidierten Hüllrohren und die Oxidation der Schmelze werden diskutiert.

Contents

Introduction

As part of the German Nuclear Safety Project, out-of-pile experiments are being conducted at the Kernforschungszentrum Karlsruhe to investigate the behavior of fuel rod simulators under severe fuel damage conditions /1,2/. These experiments provide information on the mechanisms damaging PWR fuel rods at temperatures up to 2200°C, and are part of a comprehensive Severe Fuel Damage Program being conducted at KfK /3/. In addition, these experiments directly complement integral inpile bundle tests being conducted by EG&G Idaho, Inc., in the Power Burst Facility at the Idaho National Engineering Laboratory /4/.

Earlier experiments have shown that the behavior of fuel rods at high temperatures is strongly dependent on the degree of cladding oxidation. Highly oxidized rods are very brittle and can fragment during operation and/or quench, whereas relatively unoxidized cladding melts, dissolves UO_2, and runs down the rod. The extent of oxidation depends in part on the temperature rise rate. The rise rate may be influenced by the exothermic oxidation process. If the heat of reaction is not removed fast enough, the exponential increase of the reaction with temperature may give rise to a rapid temperature escalation. Therefore, oxidation-induced temperature escalation may play an important role in determining fuel behavior. To investigate temperature escalation and processes leading to a turnaround of the escalation, a series of single rod and bundle experiments with fuel rod simulators are being performed as part of the Severe Fuel Damage Program. This report discusses the results of the nine-rod bundle test ESBU-1.

Temperature Escalation

The oxidation of zirconium in steam is an exothermic reaction which can be expressed as:

$$Zr + 2H_2O \rightarrow ZrO_2 + 2H_2 + 5.86 \times 10^5 \text{ J/mol} \qquad (1)$$

In the energy balance 10.7×10^5 J/mol are gained by the formation of the oxide and 4.81×10^5 J/mol lost by the dissociation of the two moles of H_2O. The energy potential of this reaction is remarkable. The complete oxidation of a 10.75 mm zircaloy cladding (1.5 g/cm length) in steam would deliver an energy of 9600 J/cm. Under adiabatic conditions this energy is sufficient to heat the cladding and fuel to 3700°C, including the melting of both materials.

Zirconium forms a protective layer as it oxidizes. The reaction is therefore controlled by the diffusion of oxygen through the oxide, and the reaction rate is inversely proportional to the oxide thickness.

$$\frac{dW}{dt} = K \frac{1}{W} \qquad (2)$$

where

W = kinetic parameter (oxygen uptake per unit surface area (kg/m^2), metal reacted per unit surface area (kg/m^2), or oxide thickness (m)), and
t = time (s).

The proportionality constant K has been observed to be an Arrhenius function of temperature, so that

$$K = A \exp(-B/RT)$$

where

A,B = constants to be determined experimentally, and
T = temperature of the cladding (K).

If the heat generated by the reaction can be removed from the system so that the cladding temperature remains constant, the rate of reaction will decline as 1/W. If the heat cannot be removed, or cannot be removed fast enough, and the cladding temperature rises, the exponential dependence of the reaction rate on temperature may dominate the reaction and give rise to a rapid temperature escalation. The cladding behavior will then be determined by the system boundary conditions (heat removal) and such processes that inherently limit the heat generated in the cladding.

Inherent limitations to the heat gain include (a) zircaloy consumption, (b) removal of zircaloy from the reaction, e.g. molten runoff, (c) steam starvation, and (d) and possible processes in the gas phase. The heat losses will depend on the system temperature, configuration, and available coolant. The modes of heat transport will include radiation, convection, and conduction, the relative importance of which will depend on the current state of the rod and boundary conditions.

Experiment facility

The test was performed in the NIELS facility located in the Hauptabteilung Ingenieurtechnik at KfK. Figure 1 shows side and top cross sections of the 3x3 bundle of fuel rod simulators. The simulators conformed as nearly as possible to German PWR dimensions and pitch, using zircaloy cladding of 10.75 mm outer and 9.29 mm inner diameter, UO_2 ring pellets of 9.2 mm outer and 6.1 mm inner diameter, and a tungsten heater element 6.0 mm in diameter. The overall length of the simulators was 400 mm.

To simulate the exothermic reaction energy of neighboring rods a zircaloy shroud was installed around the rod bundle. To reduce radial heat losses, the shroud was wrapped in a fiber ceramic insulation (6 mm) as shown in the inset photograph in Figure 1. Steam was inlet to the bottom of the bundle at 16 locations so that the flow would be well distributed across the bundle cross section.

Temperatures were measured by two color pyrometers and NiCr/Ni thermocouples with Inconel sheaths. Three pyrometers were located 145 mm from the bundle top on three sides of the bundle. By removing the middle portion of one of the side rods, and making holes in the shroud and insulation, the pyrometers measured temperatures on the central rod surface, a side rod surface, and the shroud surface. Figure 2 shows the locations for the thermocouples. The central rod (rod 5), side rod (6), and a corner rod (9) were each instrumented with three thermocouples, two on either side of the rod 25 mm from the upper end of the bundle, and one 50 mm from the lower end. The shroud was instrumented with three thermocouples, 50 mm from the bottom, and 25 and 145 mm from the top, respectively. The insulation was installed with three thermocouples as well, one 25 mm from the top and two 145 mm from the top (after the third and fifth layers of 1.2 mm thick insulation, respectively).

145 mm from the top of the bundle was anticipated to be the hottest location in the bundle. The thermocouples fail around 1300°C and were therefore located away from the hot spot. The thermocouples locations were chosen to provide data on the bundle axial and radial, and rod circumferential, temperature distributions. The shroud thermocouple data provides a check on the pyrometer readings at temperatures for which both functioned, and the insulation temperatures an estimate of the heat losses.

Test conduct

The test objective was to heat the rods at a mean rate of 1 to 2 °C/s. Figure 20 shows the controlled voltage (V), resultant electric current (I), and the calculated resistance (V/I) and electric power (VxI) for all eight rods heated in parallel. The plateau in voltage between 10 and 23 minutes was unintentional, and was caused by the need to repair the test rig. The resistance of tungsten increases linearly with temperature. Thus, the electric power increased nearly linearly with voltage (Figure 20).

At the beginning of the test the argon pressure was 770 Torr. A steam flow of about 1 g/s was inlet to the bundle at approximately 41 minutes. The steam flow was held constant until 66 minutes.

As shown in Figure 21 the surface temperature of the central rod increased roughly at 2°C/s until about 1700°C at which time the influence of zircaloy oxidation raised the heatup rate to around 6°C/s. The temperature reached a peak of 2250°C, then fell rapidly. Temperatures on the side rod and the shroud developed flat maximums. At 60 minutes all three temperatures showed a minimum. The electric power increased continuously throughout this period. From 60 to 64 minutes the voltage and, with this the electric power, were held constant. Finally, at 64 minutes the power was shut off and the experiment terminated.

Test results

The measured test temperatures are shown in Figures 21 through 37. Figure 21 shows the two color pyrometer measurements on the central rod, side rod and shroud at 145 mm from the upper end of the cladding, which was assumed to be near the maximum temperature. Figures 22 through 37 give the results of the thermocouple measurements on the central rod, side rod, shroud and insulation. Comparisons of two color pyrometer measurements with thermocouple measurements are given in Figures 22, 23 and 31. The posttest appearance of the bundle is shown in Figures 3-12. The preliminary results of the posttest sectioning are shown in Figures 13-19.

Temperature escalation

The pyrometer measured temperatures are compared with the electric power input in Figure 21. The temperature on the central rod shows the most pronounced peak. After an initial rise of 2°C/s the rise rate increased at 1700°C to 6°C/s. The maximum temperature reached was 2250°C, after which the temperature declined to less than 1700°C.

The center rod had the smallest net radial heat losses, due to the radiative contributions from the surrounding rods and higher local steam temperatures. This temperature therefore escalated first and showed the most pronounced escalation effect. The rapid temperature turn-around was probably due to molten zircaloy runoff from the reaction zone. The runoff is shown in the posttest pictures.

Figure 21A compares the two color pyrometer and thermocouple temperatures measured on the center rod and shroud. The shroud temperature at 145 mm from the upper end of the bundle followed the center rod temperature closely throughout much of the escalation. Only at higher temperatures did the shroud temperature escalation fall off, probably the result of greater radiation losses. The shroud temperature was clearly influenced by the exothermal reaction.

A comparison of the temperatures at 145 mm and at 25 mm from the upper end of the center rod demonstrates that the escalation behavior can be quite a local phenomenon on the same rod. The two positions were only 12 cm apart. Also, the temperature on the side rod did not rise nearly as rapidly and reached a flat peak of only about 1700°C. The greater heat losses to the surroundings reduced the reaction rate and prevented a marked temperature escalation. It is also possible that molten material from the center rod may have influenced the flow of steam and by this the escalation.

The temperature drop from 58 to 60 minutes was detected by all three pyrometers. It seems plausible that this temperature drop was associated with the above mentioned movement of molten material.

From 60 to 65 minutes all three pyrometers measured temperature increases despite a constant electric power input. Thermocouple measurements 25 mm from the bundle upper end, and 50 mm from the bundle lower end (Figures 23 and 24) showed a temperature increase at the upper end and a decrease at the lower end during this time period. Presumably the axial electric power distribution changed as a result of the melt relocating in the lower part of the bundle. A hint in this direction is the fact that the thermocouple on the center rod 50 mm from the lower end failed at about 58 minutes.

Axial temperature distribution

Time dependent temperatures at different axial positions on the central rod, side rod, and shroud are shown in Figures 22 through 24 and 28 through 31. Figures 22 and 23 show the thermocouple measurements made at the top and bottom of the rods compared to the pyrometer reading at 145 mm from the top. Figure 24 shows the thermocouple measurements on the shroud at the top, middle and bottom on an expanded scale. Top and bottom thermocouple measurements alone on an expanded scale are shown in Figures 28 through 30 for the central, side, and corner rods, respectively. Figure 31 shows all measurements made on the shroud. The middle region of the bundle was clearly the hottest area and the location where a temperature escalation occurred. On the other hand, the temperatures at 50 mm from the lower end and 25 mm from the upper end were of the same order. The measurement positions were chosen so that the thermocouples would survive the maximum temperatures if possible. The deviation from axial temperature symmetry was due to the influence of differing heat losses. The lower thermocouples were located outside the insulated region and the upper thermocouples were placed inside the insulation. At the lower positions the steam had nearly the inlet temperature, while at the upper positions the steam was superheated after flowing through the heated bundle. Figure 22 demonstrates the influence of the steam flow on the center rod. Before steam was introduced (41 minutes) the difference between the temperature 50 mm from the lower end and the temperature 25 mm from the upper end was about 75°C. After steam was inlet the temperatures were nearly the same, indicating that the axial temperature distribution had been shifted up the rod. In both cases water cooling of the copper electrodes affected the rod end temperatures.

Radial temperature distribution

The radial temperature distribution at the lower end of the bundle is shown in Figure 25. A radial temperature difference of about 100°C existed between the center rod and a corner rod, and an additional 100°C difference between the corner rod and the shroud. In the upper region of the bundle (25 mm from upper end) the radial temperature differences were quite reduced (Figure 26). After 50 minutes the temperatures for center, side and corner rods were practically the same and the shroud temperature approximately 100°C less. In the center of the bundle (Figure 21) the radial temperature distribution was extremely uneven as the central rod escalated to a temperature difference of about 600°C between it and the side rod. Later the apparent differences in the bundle were reduced as the side rod recorded a slightly higher temperature than the central rod and both were about 200°C higher than the shroud.

The temperature gradient within the insulation can be seen in Figures 32 and 33. At 50 minutes a temperature difference of 800°C existed between the shroud and the outer surface of the insulation. At the upper end of the bundle the temperature gradient within the insulation can be seen in Figure 33. A maximum difference of almost 600°C existed between the shroud and the outer surface of the insulation at 60 minutes.

Circumferential temperature gradients

Figures 35 through 37 illustrate the azimuthal temperature variation on the center, side and corner rods, respectively, at the top of the bundle. The center rod had almost no variation, while the side and corner rods showed approximately 25°C differences. The small variations were presumably due to the greater heat losses in the direction of the unheated shroud.

Steam temperature and rod heat transfer

The steam exit temperature was measured between a side rod, corner rod, and the shroud (Figure 2) as shown in Figure 27 with the measured shroud and rod temperatures. These measurements permit an estimation of the rod surface heat transfer at this location and the convective and radiative components of it. The following is an approximate calculation whose purpose is to determine if the observed temperatures correspond to common sense. At 60 minutes into the experiment most of the heat generation due to the zircaloy/steam reaction had already been generated. The electric power to the bundle was 8 kW, or 1 kW per heated rod. The power generated in the tungsten heater is related to the resistivity, rod dimensions, and electric current as follows:

$$q = \frac{\rho(T) l I^2}{\pi r_\omega^2} \qquad (4)$$

where q = electric power (W)

$\rho(T)$ = temperature dependent resistivity (Ωm)

T = temperature (K)

l = length of rod at T (m)

I = electric current (A)

r_ω = heater radius (m)

Solving for the resistivity (Figure 20 data)

$$\rho(T) = \frac{(1000\ \text{W})\ \pi\ (.003\ \text{m})^2}{(0.40\ \text{m})\ \ (312.5\ \text{A})^2}$$

$$I = 7.2 \times 10^{-7}\ \Omega\text{m}$$

which corresponds to a tungsten temperature of around 2100°C. This is an effective tungsten temperature over the whole rod length. The local tungsten temperature at the elevation of the steam temperature measurement can be estimated as follows: The difference between heater temperature and rod surface temperature can range from 200 to 500°C, depending on the heater temperature and boundary conditions. For a measured rod surface temperature of 1200°C (Figure 27, 60 minutes) an estimate of 1450°C for the tungsten temperature is reasonable. This corresponds to a resistivity of about 5 x 10^{-7} Ωm, or a local linear power of

$$q' = \frac{(5 \times 10^{-7}\ \Omega m)\ (1\ m)\ (312.5\ A)^2}{\pi\ (0.003\ m)^2}$$

$$= 1700\ \frac{W}{m}$$

The convective and radiative heat transfer from the rod to the steam and shroud can be described as

$$q = hA\ (T_r - T_{st}) + A\varepsilon\sigma\ (T_r^4 - T_s^4) \qquad (5)$$

where
h = convective heat transfer coefficient $(\frac{W}{m^2 \cdot K})$
A = area $2\pi r_c l$
r_c = cladding radius (m)
T_r = rod temperature (K)
T_{st} = steam temperature (K)
T_s = shroud temperature (K)
ε = effective emmissivity (-)
σ = Boltzmann's constant 5.6678 E-8 $(\frac{W}{m^2 \cdot K^4})$

The convective heat transfer coefficient h can be calculated from the Dittus-Boelter correlation /5/ for forced convection:

$$h = 0.023\ \frac{k}{D_e}\ (Pr)^{0.4}\ (Re)^{0.8} \qquad (6)$$

where
k = thermal conductivity of fluid $(\frac{W}{m \cdot K})$
D_e = hydraulic diameter (m)
Pr = Prandtl number (-)
$Re = \frac{GD_e}{\mu}$ = Reynolds number (-)
G = mass flux $(\frac{kg}{m^2 \cdot s})$
μ = fluid viscosity (Pa·s)

Using the given data plus the following properties of steam at 1 bar and 800°C /6/,

$$k = 0.110 \frac{W}{m \cdot K}$$
$$Pr = 0.87$$
$$= 4.12 \times 10^{-5} \ (Pa \cdot s)$$
$$D_e = 0.0093 \ m,$$

then
$$Re = \frac{(9)\ (.000107)\ (.0093)}{(.044^2 - 9\ \pi\ (.005375)^2)\ (4.12 \times 10^{-5})} = 195$$

and
$$h = \frac{(.023)\ (0.110)}{(.0093)}\ (0.87)^{0.4}\ (195)^{0.8} = 17 \frac{W}{m^2 \cdot K}$$

The observed temperatures (Figure 27, 60 minutes) were T_r = 1175°C, T_s = 1075°C, and T_{st} = 850°C. Using these temperatures, the estimated local linear power of 1700 $\frac{W}{m}$ and the estimated convective heat transfer coefficient of 17 $\frac{W}{m^2 \cdot K}$, equation (5) can be solved for the effective emmissivity

$$\varepsilon = \frac{1700 - (15)\ (2\pi r_c)\ (T_r - T_{st})}{2\pi r_c\ \sigma\ (T_r^4 - T_s^4)} = 0.7$$

The data for ZrO_2 emmissivity at high temperatures vary between 0.6 and 0.8. The particular effects of geometry have not been considered. Therefore, the measured temperatures appear consistent and reasonable. Of the estimated 1700 W/m local linear power, roughly 180 W/m was removed by convection and 1520 W/m by radiation.

Heat balance

The radial distribution of temperature in the shroud and insulation is shown in Figures 32 and 33 for the middle and top of the bundle respectively. Figure 34 illustrates the axial distribution on the surface of the insulation. Using these data and the steam temperature data of Figure 27, on estimate of the overall heat distribution can be made. Again, using 60 minutes as an example, the temperature drop across the insulation at the top of the bundle was (Figure 33)

$$\Delta T_{top} = 1075^{o}C - 500^{o}C = 575^{o}C$$

and at the middle of the bundle (Figures 21 and 34)

$$\Delta T_{mid} = 1550^{o}C - 750^{o}C = 800^{o}C$$

The insulation thickness L was 0.00625 m and had a thermal conductivity k of 0.24 $\frac{W}{m \cdot K}$. Thus the heat fluxes can be estimated from

$$q'' = - \frac{k \Delta T}{L} \qquad (7)$$

where q'' = heat flux $(\frac{kW}{m^2})$

$$q''_{top} = 22 \frac{kW}{m^2}$$

$$q''_{mid} = 31 \frac{kW}{m^2}$$

Assuming roughly half the surface was at the higher ΔT and half at the lower, the radial heat losses can be estimated from the bundle dimensions

$q_{top} = 0.8$ kW

$q_{mid} = 1.1$ kW

The heat losses by convection can be estimated from,

$$q_{con} = W \, Cp \, \Delta T_{st}$$

where w = coolant mass flow rate $(\frac{kg}{s})$

C_p = coolant specific heat capacity $(\frac{J}{kg \cdot K})$

T_{st} = coolant temperature rise (K)

The coolant exit temperature was 850°C. Assuming an inlet temperature of 120°C and evaluating C_p at the average temperature,

$$q_{con} = (9)\ (1.07 \times 10^{-4})\ (2150)\ (730) = 1.5 \text{ kW}$$

At 60 minutes, the bundle consumed 8 kW electric power. Subtracting the convective and radial heat losses, 4.6 kW remain to be accounted for by transient heating, axial conduction, heats of fusion, and so on. The above estimates are rough, but serve to illustrate that no one heat loss mechanism dominated the bundle behavior and that all should be considered in a comprehensive analysis.

Posttest appearance

The appearance of the bundle following the test is shown in Figure 3 before removing the insulation. The insulation and shroud were still intact following the test. However, both were severely embrittled, as the removal of the insulation from the shroud showed. The insulation, originally a flexible mat, broke into many pieces. The careful removal of the insulation also broke off pieces of the shroud as shown in Figure 4. The shroud was severely oxidized over the center region of the bundle and therefore broke away in several places revealing the fuel rod simulators.

Figures 5 and 6 show the fuel rod simulators after removal of the shroud. The cladding from all nine rods has melted over the center portion of the bundle, liquefied some fuel, flowed down the rods, and frozen in a solid mass near the bottom of the bundle that substantially blocked the coolant flow channels. The shroud adhered to the refrozen mass. In Figure 6 the lower portion of the shroud was removed as well as possible, revealing metallic looking zircaloy near the steam inlet changing to oxidized zircaloy near the blockage lower end. The upper end of the bundle contained intact but oxidized zircaloy cladding. In the middle region only the remains of pellets that stuck to the tungsten rod can be seen.

Figures 7 and 8 detail the appearance of the lower bundle region. Oxide spalling is evident as is refrozen drops of the liquefied material. The refrozen melt shows poor wetting of the solid surface as indicated by the large wetting angles and small contact areas. Melt viscosity, oxygen content, and relatively cold fuel rod simulators probably influenced the refreezing behavior in this region.

Figures 9 through 11 illustrate the appearance of the blocked region from above. The refrozen melt has a smooth surface and wet the remaining simulators rather well (small wetting angle and large contact surface). The melt interacts with the oxidized fuel rod simulators and steam. The composition of the melt and these interactions will be the primary subject of the posttest examination.

A large amount of powdery rubble, not shown in the previous photographs, was found on top of the blockage. The rubble was probably fuel that fractured during cooldown. Figure 12 shows rubble remnants on the experiment support structures. Composition and sieve analysis of the rubble will be included in the posttest examination.

Posttest sectioning

The bundle was encapsulated in epoxy after the test and cut into sections as shown in Figure 13. Figure 14 shows a summary of the bundle cross section appearances in the blocked region and Figures 15 through 19 show enlargements of the cross sections. Note that the photographs at 15 mm (Figure 19), 119 mm (Figure 15), and 129 mm (Figure 15) are left-right reversed with respect to the other photographs because they were taken from the bottom rather than top of the sections. The photographs at 119 and 116 mm are of the bottom and top surfaces, respectively, of adjacent cross sections and are separated only by the 3 mm saw kerf.

The right hand photograph in Figure 15 shows the cross section at 119 mm, corresponding to the bottom of section 2. The cross section is less than 10 mm from the surface of the refrozen melt. The white circular areas are the tungsten heaters, surrounded by black UO_2 ring pellets. The outer radii of the UO_2 ring pellets have been reduced to about 4.2 mm from 4.6 mm, indicating some dissolution of UO_2 by liquid zircaloy. The cladding has essentially disappeared. Only faint rings at the original cladding boundaries can be recognized for some rods. A large coherent lump of refrozen melt has filled the space between pellets and shroud.

The refrozen material is molten zircaloy from the high temperature region of the bundle which has dissolved UO_2 pellets. In the test the temperature rise rate was so fast that only a thin ZrO_2 layer formed on the cladding. When the melting temperature of zircaloy was reached, the inner unoxidized cladding melted. Molten zircaloy ensures good contact between zircaloy and UO_2 so that large scale dissolution can begin. The oxide layer was apparently too weak to keep the melt enclosed. The molten zircaloy ran down, further dissolving UO_2. The first droplets refroze in the lower part of the bundle. Melt running down later refroze on top of the earlier refrozen droplets. The appearance of the cross section at 119 mm indicates that at that elevation the melt refroze at the same time.

Microprobe analysis of the melt have shown that the refrozen melt (at relatively low oxygen contents) consists of three phases: (a) α-Zr(O), (b) a uranium rich (U,Zr) alloy, and (c) $(U,Zr)O_2$ mixed oxide. The results of the posttest investigations will be presented in a future KfK report.

The hole in upper left part of the cross section at 119 mm was the only channel left open for steam flow. The dark seam around this channel is melt oxidized by steam, forming a $(U,Zr)O_2$ mixed oxide. Similar oxidation of the melt can be recognized in Figures 16 and 17 (116-86 mm).

With decreasing elevation the hole size increases and more oxidized cladding forms part of the boundary of the channel. At the 106 mm elevation a second hole formed in the lower partion of the cross section. A comparison to the 116 mm cross section shows that no steam flow was possible there. Stagnant steam or perhaps a hydrogen bubble may have formed there. As a consequence only minor oxidation is evident.

The first evidence of oxidized cladding appears at 106 mm, progressing from top to bottom. Above 106 mm the oxidized cladding appears to have been completely dissolved by the melt. Below 106 mm the cladding attack decreases with elevation and temperature.

Figure 17 shows evidence that the interaction history was not the same for different regions of the same cross section. The melt between the four rods on the upper left has not appreciably interacted with the oxidized cladding, in contrast to the melt in the lower regions of the photographs. The structure of the different cross sections indicates that droplets of varying lengths have refrozen at different times in the channels between the rods. The arriving melt may have also had varying temperatures. The later the melt refroze in a particular position, the longer the cladding oxidation time was and the shorter the melt interaction time was.

The center rod at 96 mm (Figure 17) illustrates four distinct cladding regions, beginning clockwise from the lower right: (a) strong cladding/melt interaction such that the two are visually indistinguishable, (b) weaker cladding/melt interaction, with the interface still visible, (c) oxidized cladding/melt contact with very little interaction, and (d) severely oxidized cladding with no melt contact.

Figure 18 at 76 mm shows severe oxidation of all nine rods. As is apparent along the edges of the melt, most of the oxidation must have occurred after the melt ran down and refroze. Figure 18 at 66 mm and Figure 19 at 51 mm show successively less oxidation until, in Figure 19 at 15 mm, almost no oxidation is visible. Since the steam flow was obviously ample, the temperatures in this region must have been much lower.

Discussion

Five interesting and important modes of material behavior occurred during test ESBU-1: (a) temperture escalation due to the zircaloy/steam reaction, (b) zircaloy melting, fuel liquefaction, and runoff, (c) melt interaction with steam, (d) melt interaction with oxidized zircaloy, and (e) fuel fracturing. It is clear from the temperature data that the central rod escalated first, and from the posttest appearance that the fuel fracturing occurred during cooldown. However, the sequence of events inside the bundle during the approximately 17 minutes from escalation until power shut down are not known in detail.

The temperature histories and blockage sections suggest that melting, runoff, interaction and refreezing did not happen in that sequence simultaneously through out the bundle. Rather, portions of the bundle melted, ran down and refroze before other portions. Thus, the boundary conditions must have changed continously.

In particular, the steam flow area must have been gradually reduced during the experiment. Whether this altered the actual mass flow rate was not determined. A bundle blockage could have two competing effects on bundle behavior. On one hand, reduced steam would limit the subsequent zircaloy/steam reaction. On the other hand, the reduced flow would limit an important source of cooling. Which effect is more important would depend on how much fresh zircaloy remained to be reacted.

In summary, the material behavior modes can effect the system boundary conditions which in turn alters the material behavior. Future experiments will attempt to record the timing and nature of events as they occur.

Acknowledgment

The authors would particularly like to thank Mr. Albiez for the data processing and graph preparation, Mr. Brand for taking the photographs and Mrs. Ivanitsch for her careful typing of the manuscript. We are grateful to Mr. Frank Panisko for arranging the delivery of the zircaloy for the shroud.

References

1. S. Hagen, H. Malauschek, K.P. Wallenfels, S.O. Peck
   Temperature Escalation in PWR Fuel Rod Simulators due to the Zircaloy/Steam Reaction: Tests ESSI 1-3, Test Results Report,
   KfK-3507, 1983

2. S. Hagen, H. Malauschek, K.P. Wallenfels, S.O. Peck
   Temperature Escalation in PWR Fuel Rod Simulators due to the Zircaloy/Steam Reaction: Tests ESSI 4-11, Test Results Report,
   KfK-3557, 1983

3. A. Fiege,
   "Severe Fuel Damage Research in Germany - A Review of the KfK/PNS Program,"
   International Meeting on Light Water Reactor Severe Accident Evaluation,
   Cambridge, Massachusetts, USA, August 28 - September 1, 1983.

4. P.E. MacDonald, G.P. Marino,
   Power Burst Facility Severe Fuel Damage Test Program,
   EG&G Idaho, Inc., EGG-J-04282, October 1982.

5. F.W. Dittus, L.M.K. Boelter,
   "Heat Transfer in Automobile Radiators of the Tubular Type,"
   University of California Publications 2(1930) pp 443-461.

6. ASME Steam Tables, Fourth Edition, 1979.

List of figures

Fig. 21: Temperatures on the central rod (Z), side rod (N) and shroud (S) 145 mm from the upper end of cladding compared to the electric power input for ESBU-1

Fig. 22: Temperatures on the central rod at 50 mm from the lower end (LO) and 25 mm (UPB and UPD) and 145 mm (MI) from the upper end: ESBU-1

Fig. 23: Temperatures on the side rod at 50 mm from the lower end (LO) and 25 mm (UPB and UPD) and 145 mm (MI) from the upper end: ESBU-1

Fig. 24: Temperatures on the shroud at 50 mm from the lower end (LO) and 25 mm (UP) and 145 mm (MI) from the upper end of the cladding: ESBU-1

Fig. 25: Temperatures on the central rod (R5) side rod (R6) corner rod (R9) and shroud (S) at 50 mm from the lower end of the cladding: ESBU-1

Fig. 26: Temperatures on the central rod (R5) side rod (R6) corner rod (R9) and shroud (S) at 25 mm from the upper end of the cladding: ESBU-1

Fig. 27: Temperatures on the central rod (R5) side rod (R6) and shroud (S) at 25 mm from the upper end in comparison to the steam temperature (ST)

Fig. 28: Temperatures on the central rod at 50 mm from the lower end (LO) and 25 mm from the upper end (UP) of the cladding: ESBU-1

Fig. 29: Temperatures on a side rod (R6) at 50 mm from the lower end (LO) and 25 mm from the upper end (UP) of the cladding: ESBU-1

Fig. 30: Temperatures on a corner rod (R9) at 50 mm from the lower end (LO) and 25 mm from the upper end (UP) of the cladding: ESBU-1

Fig. 31: Temperatures on the shroud at 50 mm form the lower end (LO) and 25 mm (UP) and 145 mm (MI) from the upper end of the cladding: ESBU-1

Fig. 32: Temperatures at 145 mm from the upper end of the cladding on the shroud at 2.5 mm (I2) and 6.25 mm (I5) within the fiber ceramic insulation

Fig. 33: Temperatures on the shroud (s) and on the surface of the insulation (I) at 25 mm from the upper end of the cladding: ESBU-1

Fig. 34: Temperatures on the surface of the insulation at 25 mm (UP) and 145 mm (MI) from the upper end of the cladding: EESBU-1

Fig. 35: Temperatures on two opposite sides (UPB and UPD) of the central rod at 25 mm from the upper end of the cladding: ESBU-1

Fig. 36: Temperatures on two opposite sides (UPB and UPD) of the side rod (R6) at 25 mm from the upper end of the cladding: ESBU-1

Fig. 37: Temperatures on two opposite sides (UPI adn UPA) of a corner rod (R9) at 25 mm from upper end of the cladding: ESBU-1

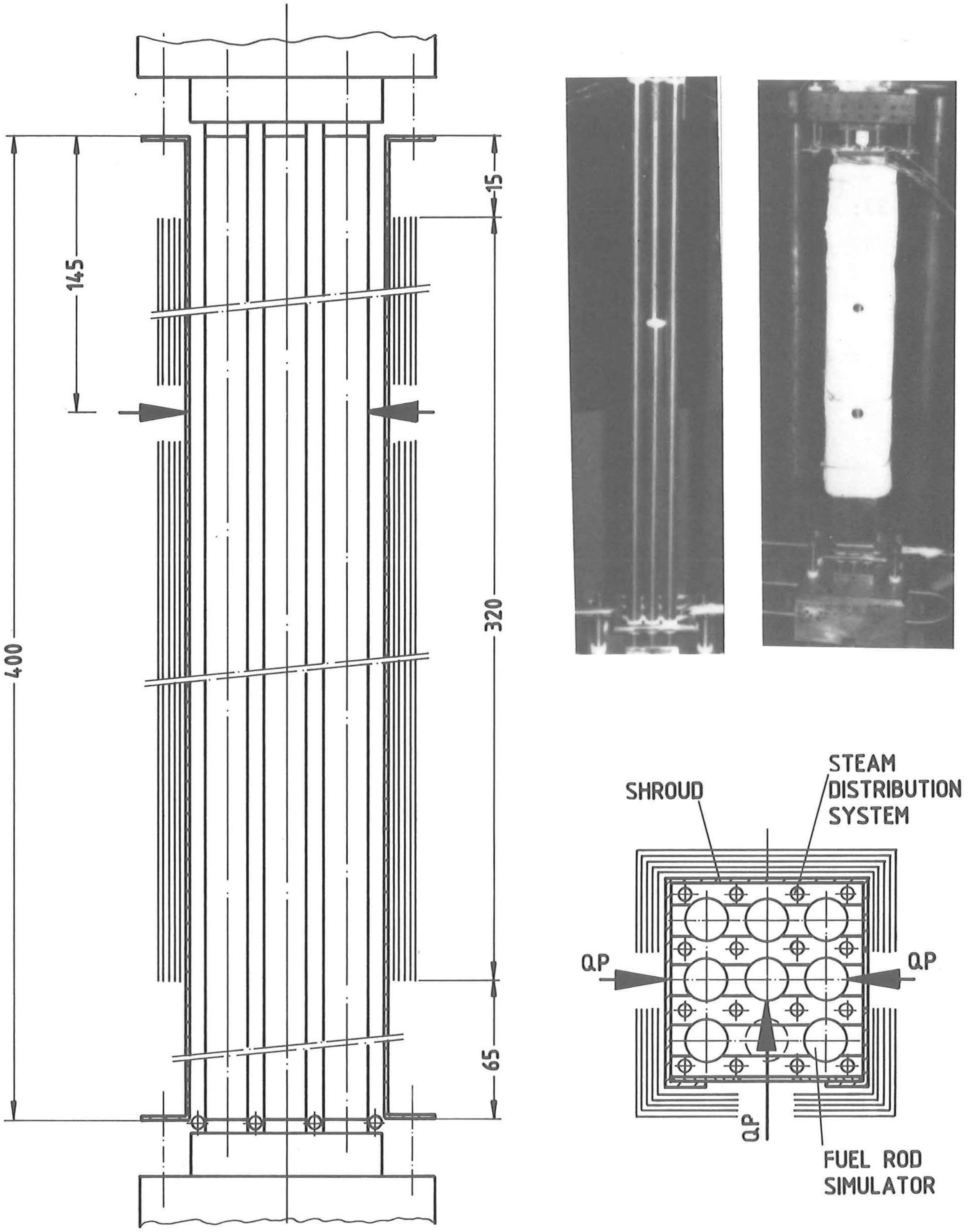

HAGEN ET AL, KFK-REPORT 3508 PNS KfK IT

FIGURE 1: ESBU-1 AXIAL AND RADIAL CROSS SECTIONS AND THE LOCATIONS OF THE TWO-COLOR PYROMETERS

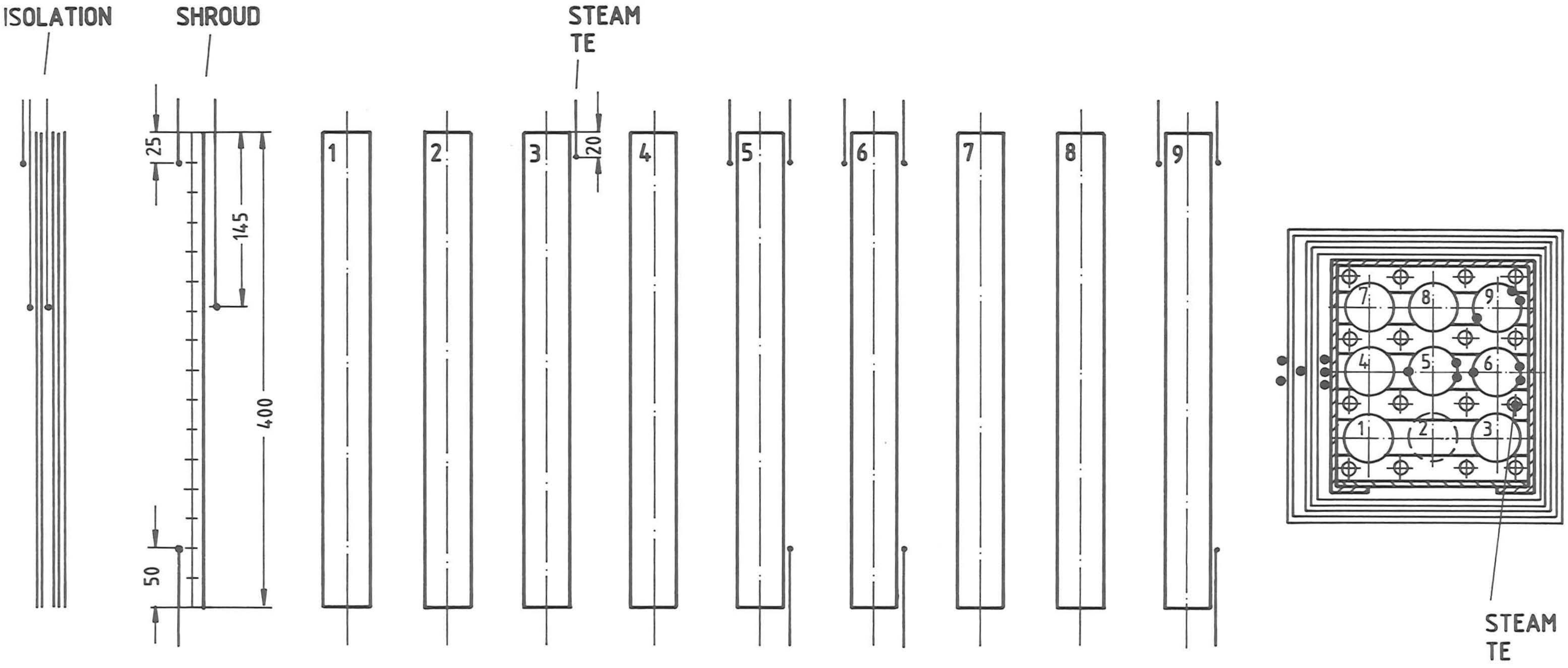

HAGEN ET AL. KFK-REPORT 3508

PNS KfK IT

FIGURE 2: AXIAL AND RADIAL POSITIONS OF THE THERMOCOUPLES OF TEST ESBU-1

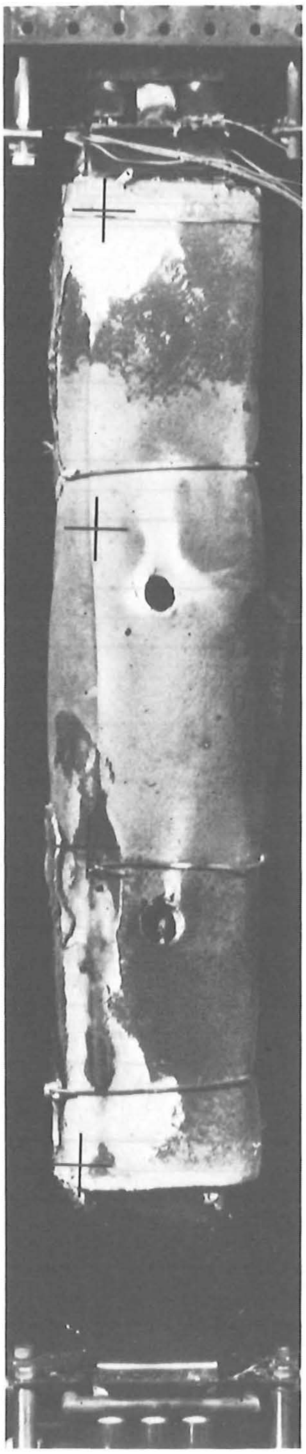

FIGURE 3: BUNDLE ESBU-1 WITH INSULATION AFTER THE TEST

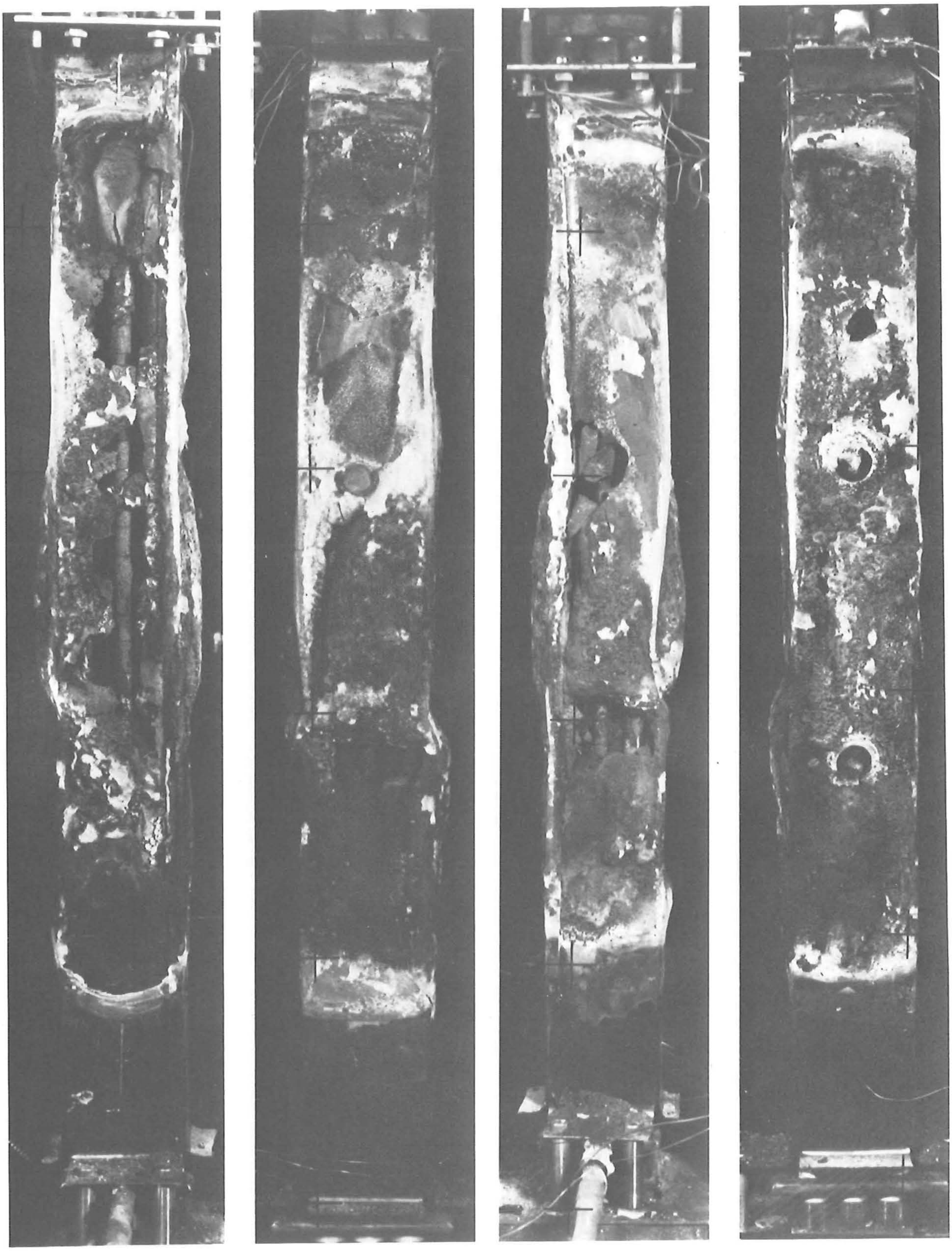

HAGEN ET AL. KFK-REPORT 3508 PNS IT

FIGURE 4: FOUR ORIENTATIONS OF THE ESBU-1 SHROUD AFTER REMOVAL OF THE INSULATION

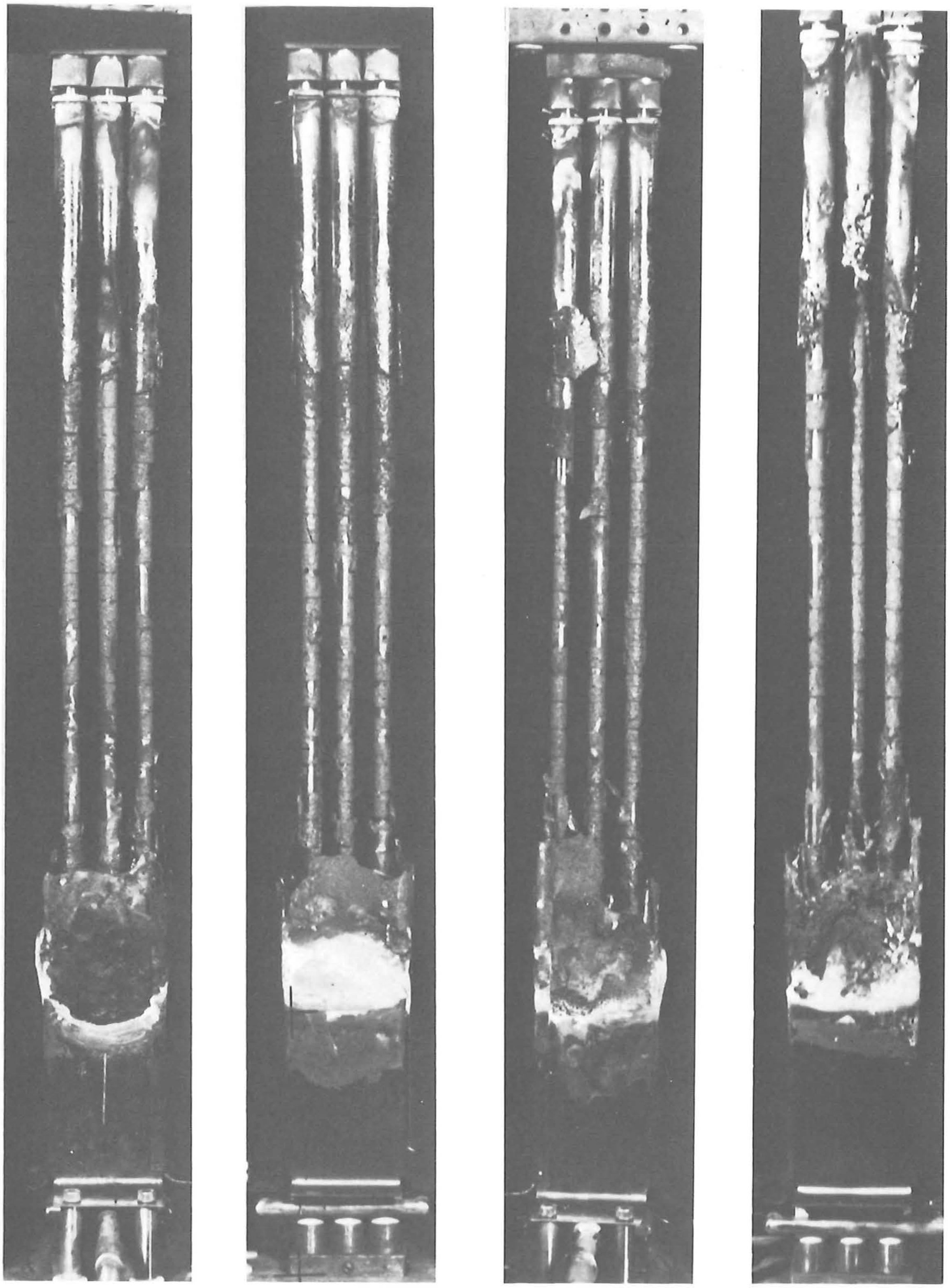

HAGEN ET AL, KFK-REPORT 3508 PNS KfK IT

FIGURE 5: 3×3 BUNDLE OF ESBU-1 AFTER REMOVAL OF THE UPPER PART OF THE SHROUD

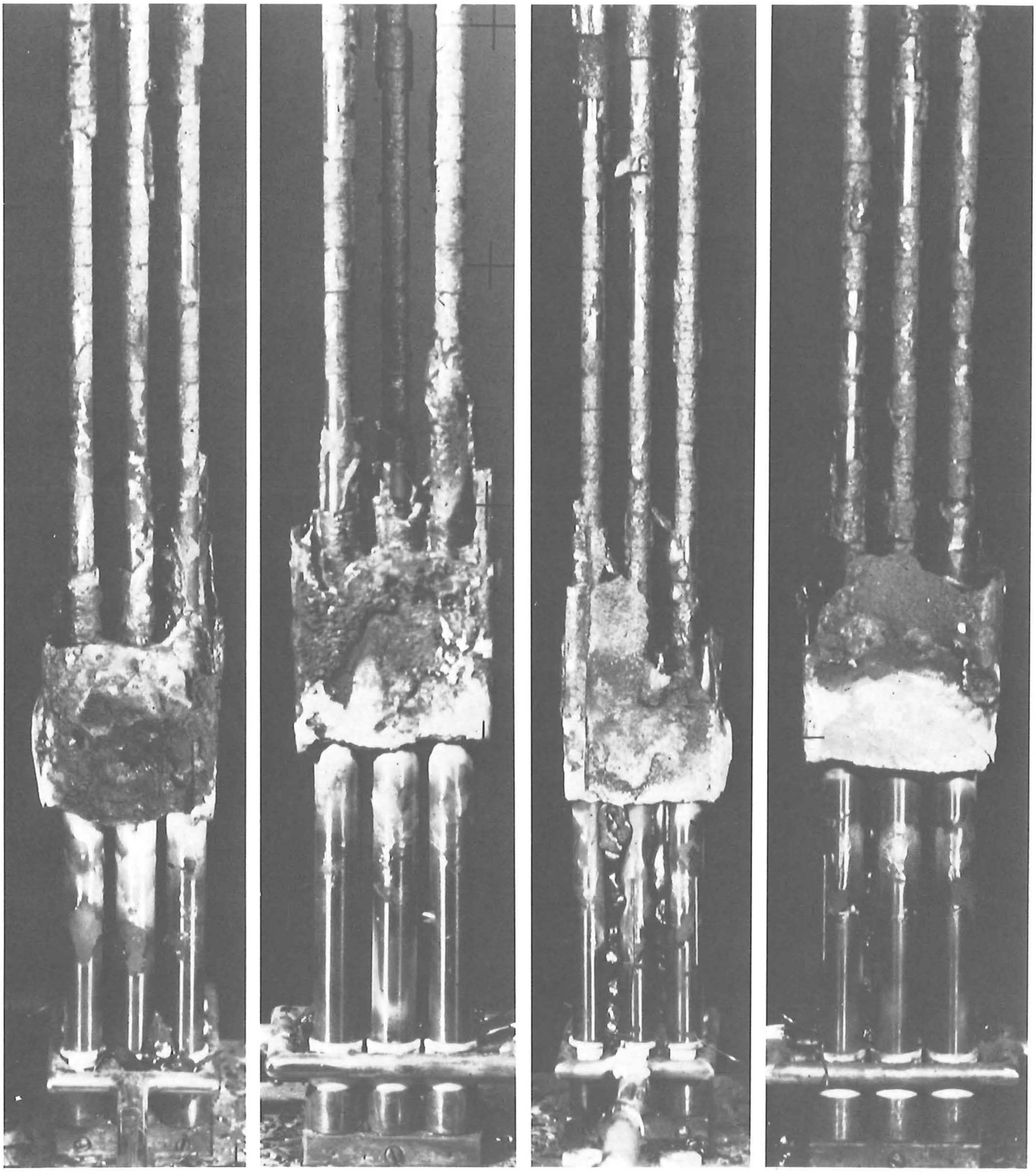

HAGEN ET AL. KFK-REPORT 3508

PNS KfK IT

FIGURE 6: LOWER REGION OF ESBU-1 AFTER REMOVAL OF THE SHROUD

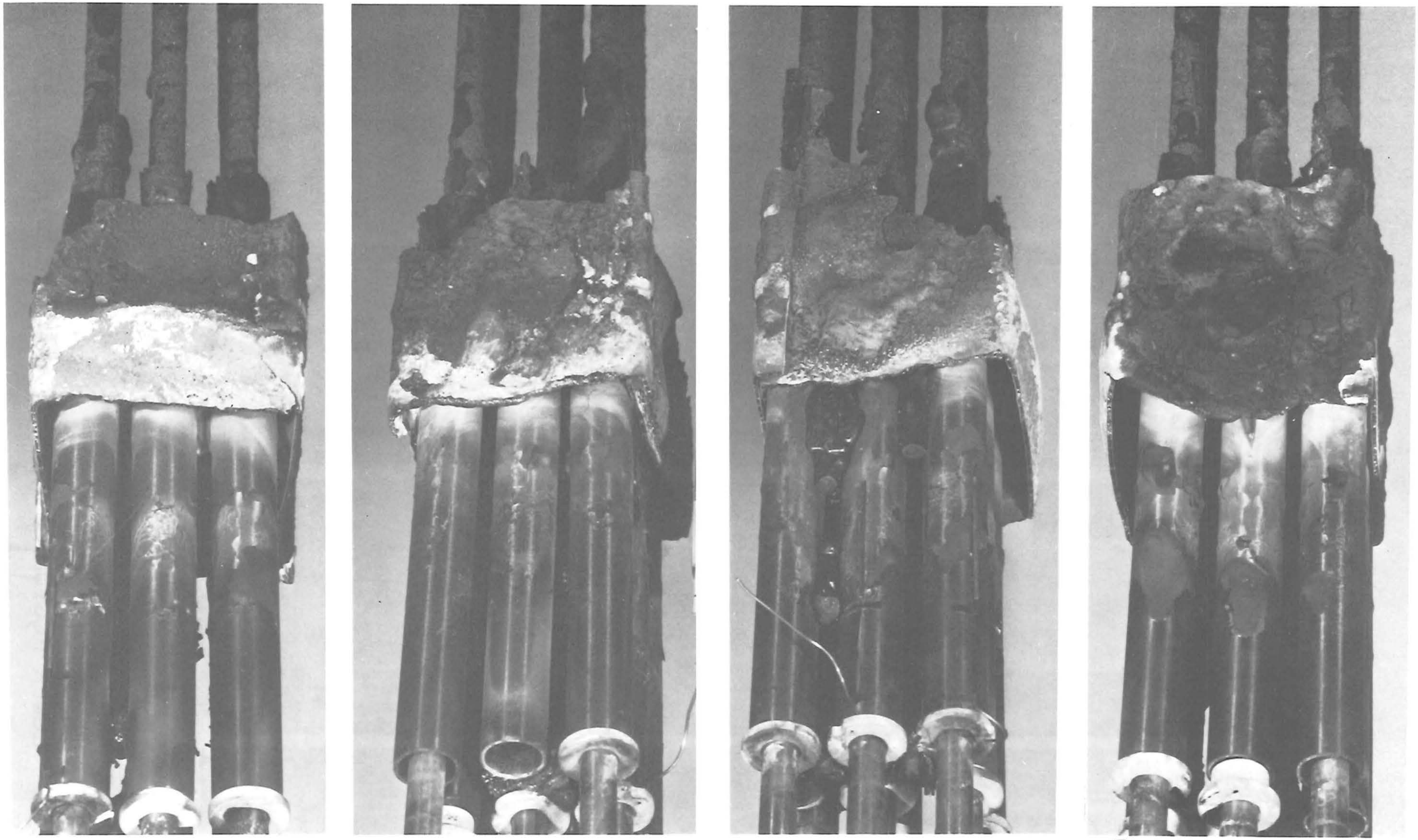

HAGEN ET AL. KFK-REPORT 3508 PNS KfK IT

FIGURE 7: APPEARANCE OF THE BLOCKED REGION OF ESBU-1 AS SEEN FROM BELOW

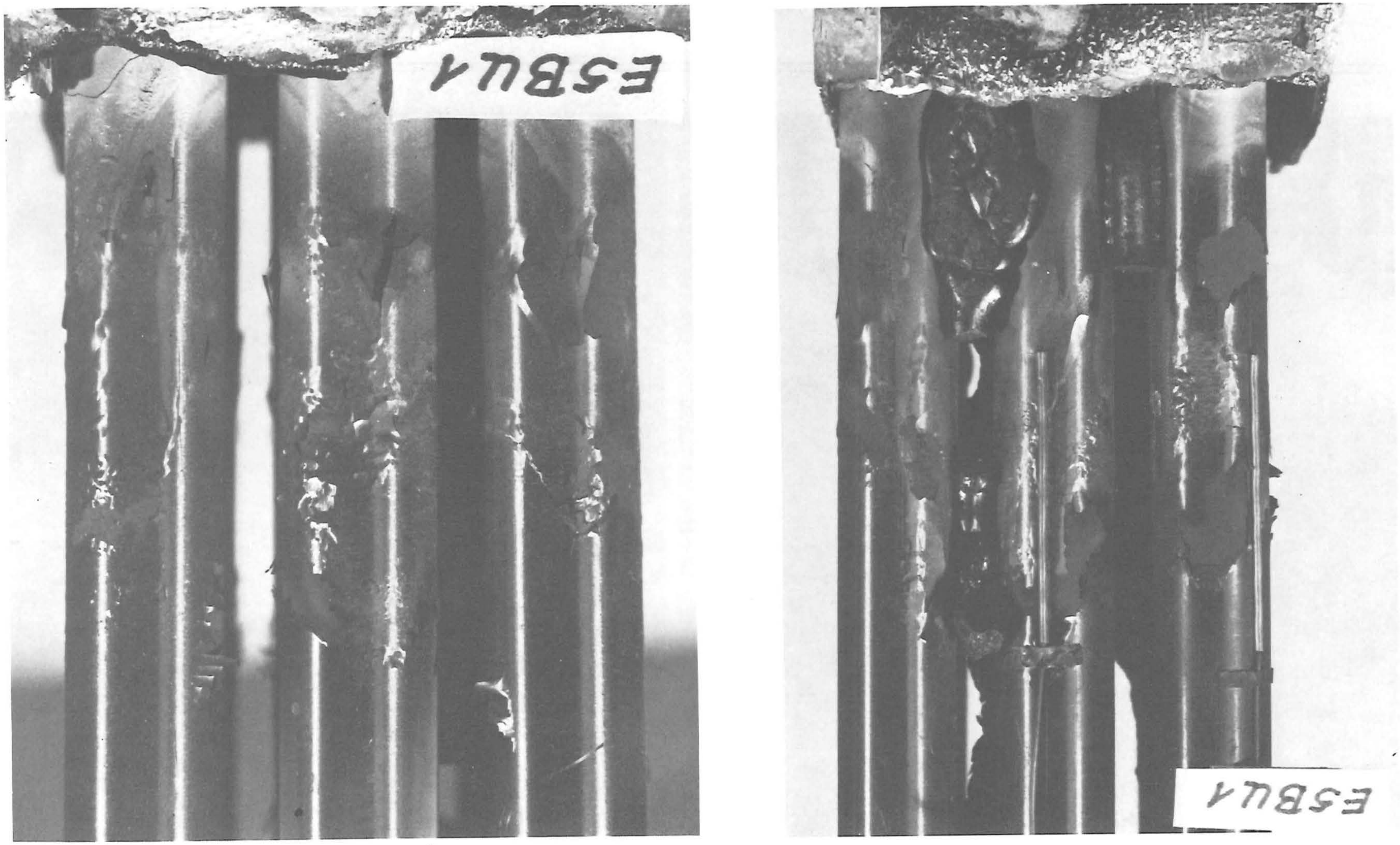

FIGURE 8: DETAILS OF OXIDE SPALLING AND REFROZEN MELT OF ESBU-1 BELOW BLOCKED REGION

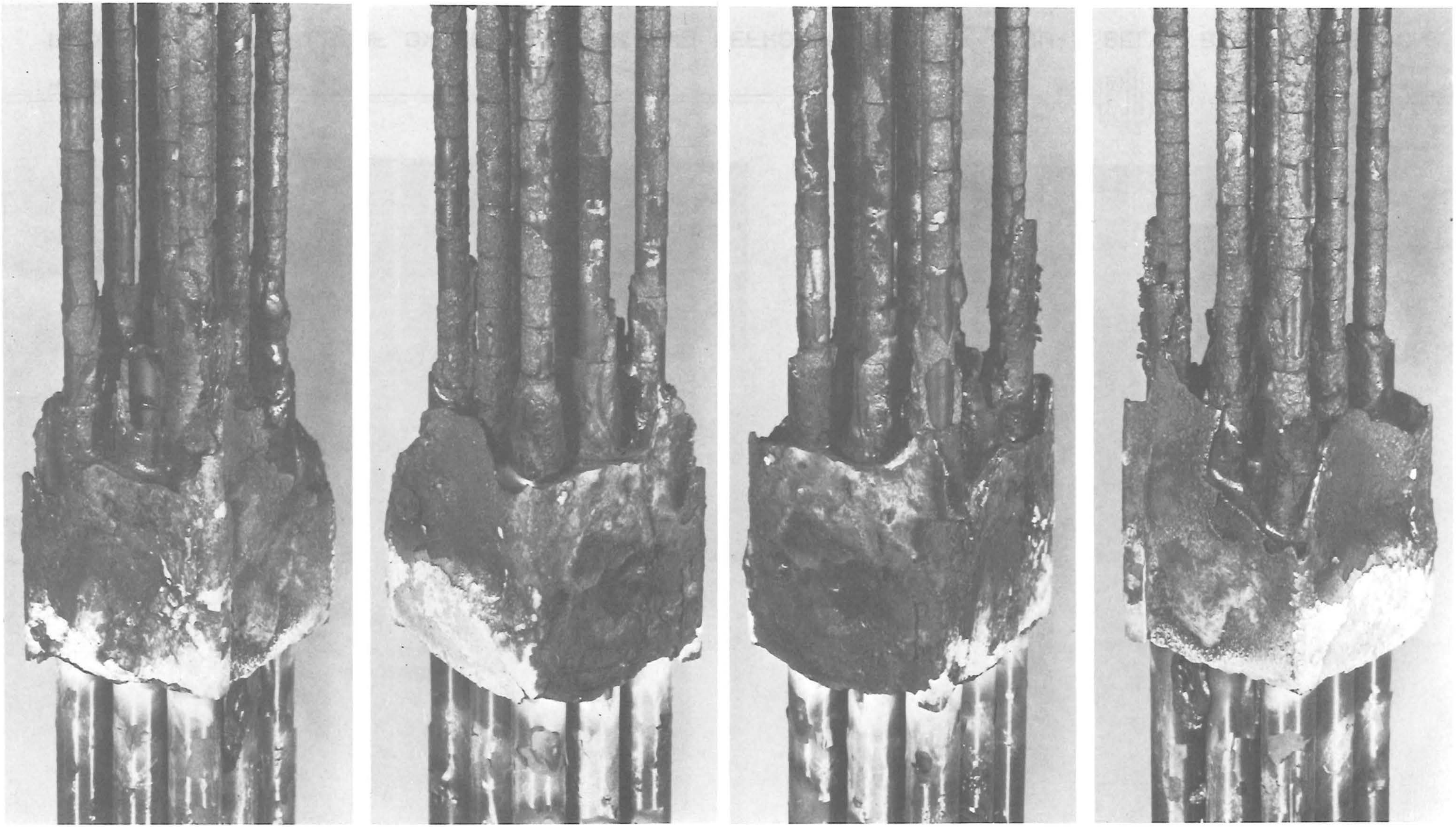

FIGURE 9: APPEARANCE OF THE BLOCKED REGION OF ESBU-1 AS SEEN FROM ABOVE

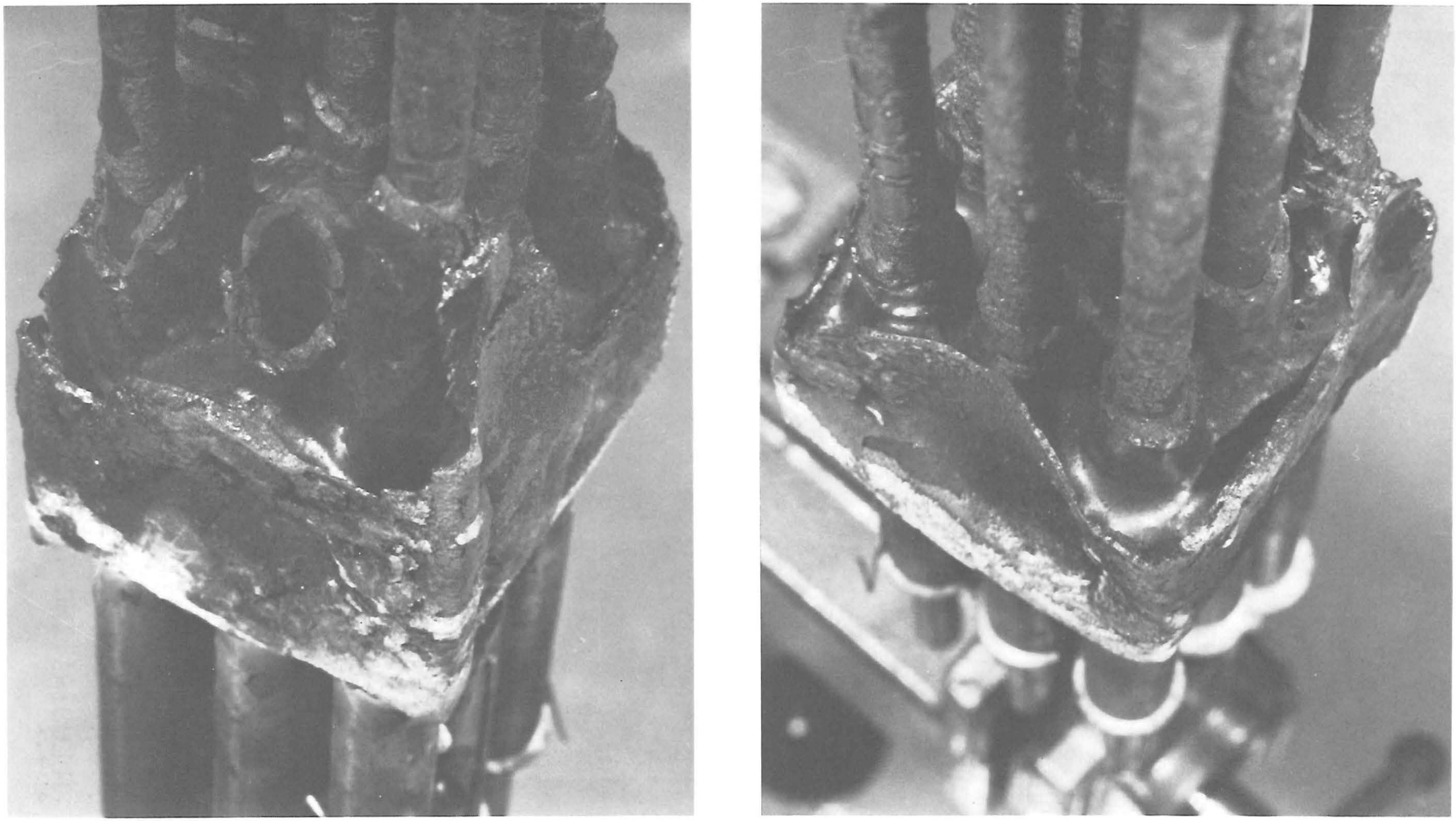

FIGURE 10: DETAILS OF BLOCKED REGION OF ESBU-1 SHOWING THE REFROZEN MELT FROM ABOVE

FIGURE 11: ENLARGEMENT OF THE BLOCKED REGION OF ESBU-1 ILLUSTRATING THE WETTING BEHAVIOR OF THE MELT

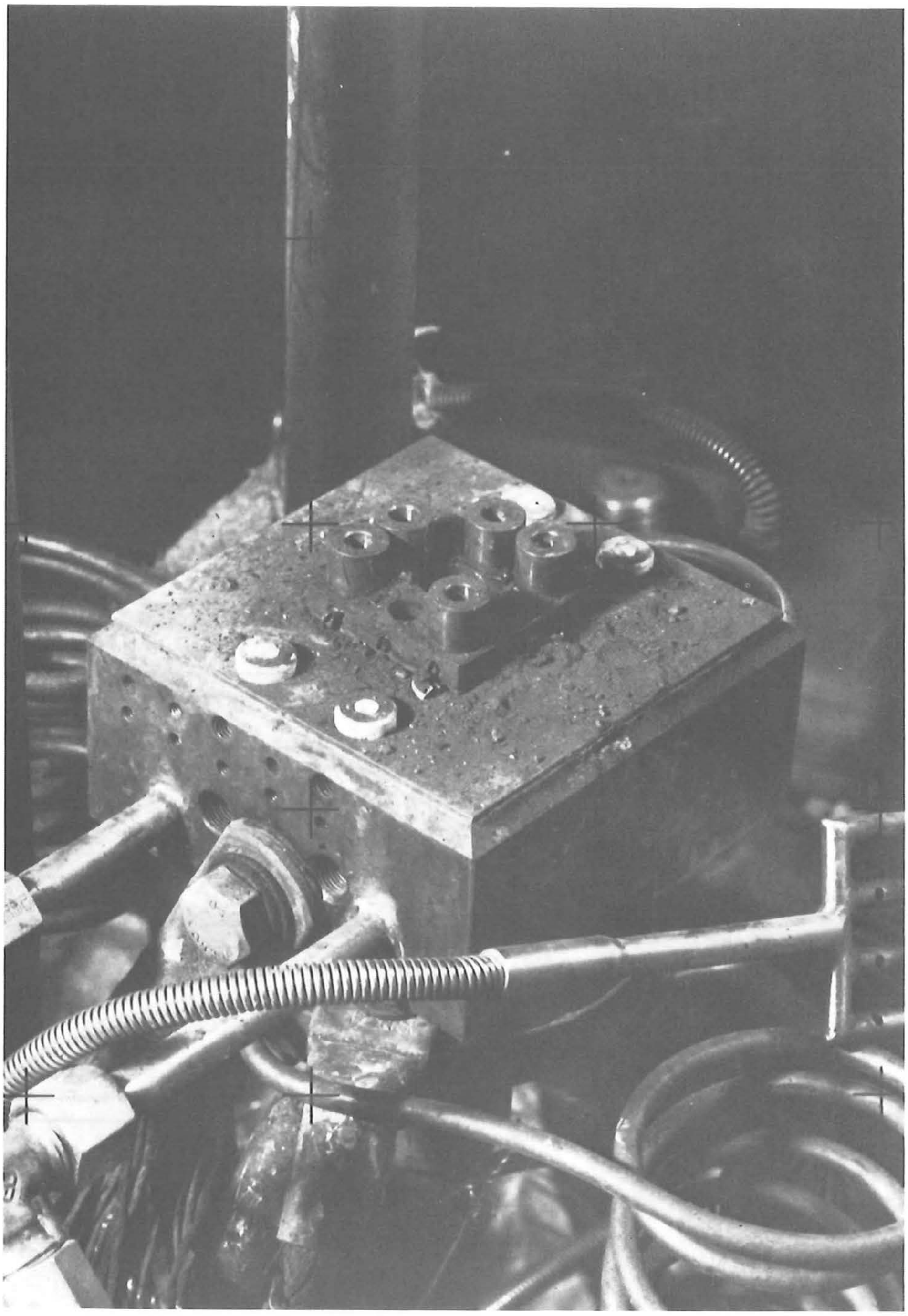

FIGURE 12: POWDER REMNANTS WHICH WERE LYING IN LARGE AMOUNTS ON TOP OF THE FROZEN LUMP

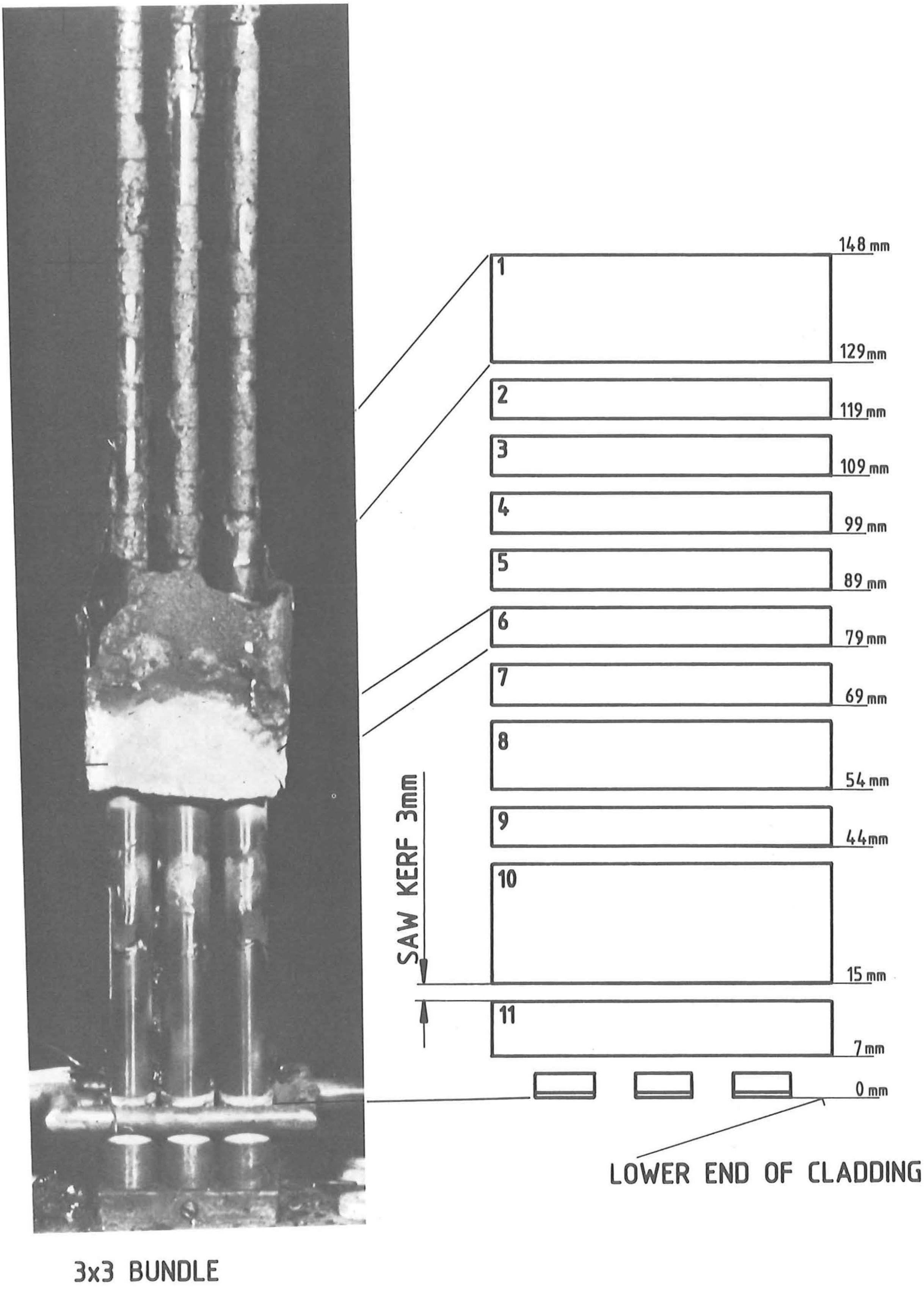

FIGURE 13: SCHEMATIC DIAGRAM SHOWING AXIAL ELEVATIONS OF THE ESBU-1 CROSS SECTIONS.

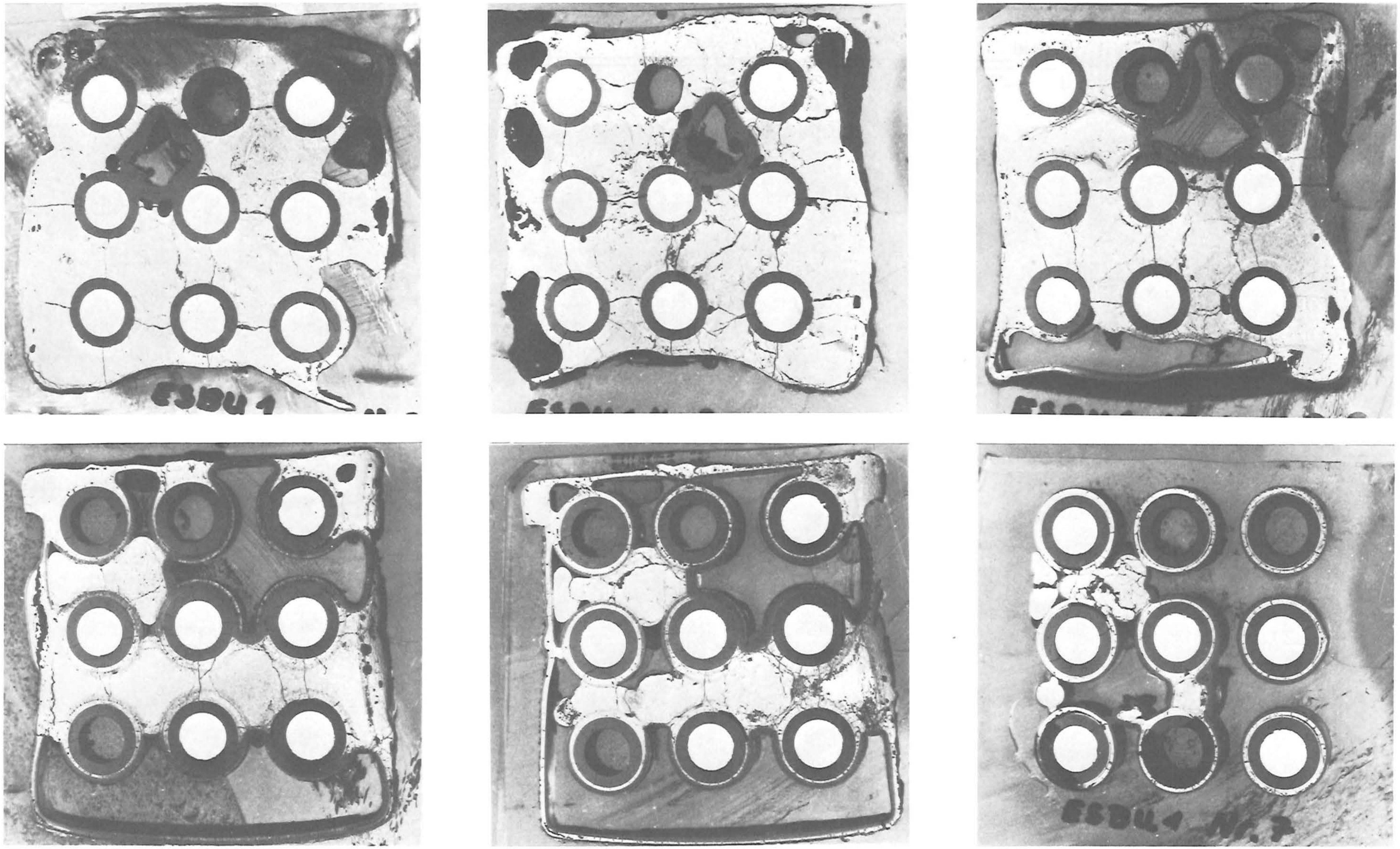

119 mm 116 mm 106 mm

96 mm 86 mm 76 mm

HAGEN ET AL. KFK-REPORT 3508 PNS KfK IT

FIGURE 14: BUNDLE CROSS SECTION SUMMARY. THE FOLLOWING FIGURES GIVE DETAIL

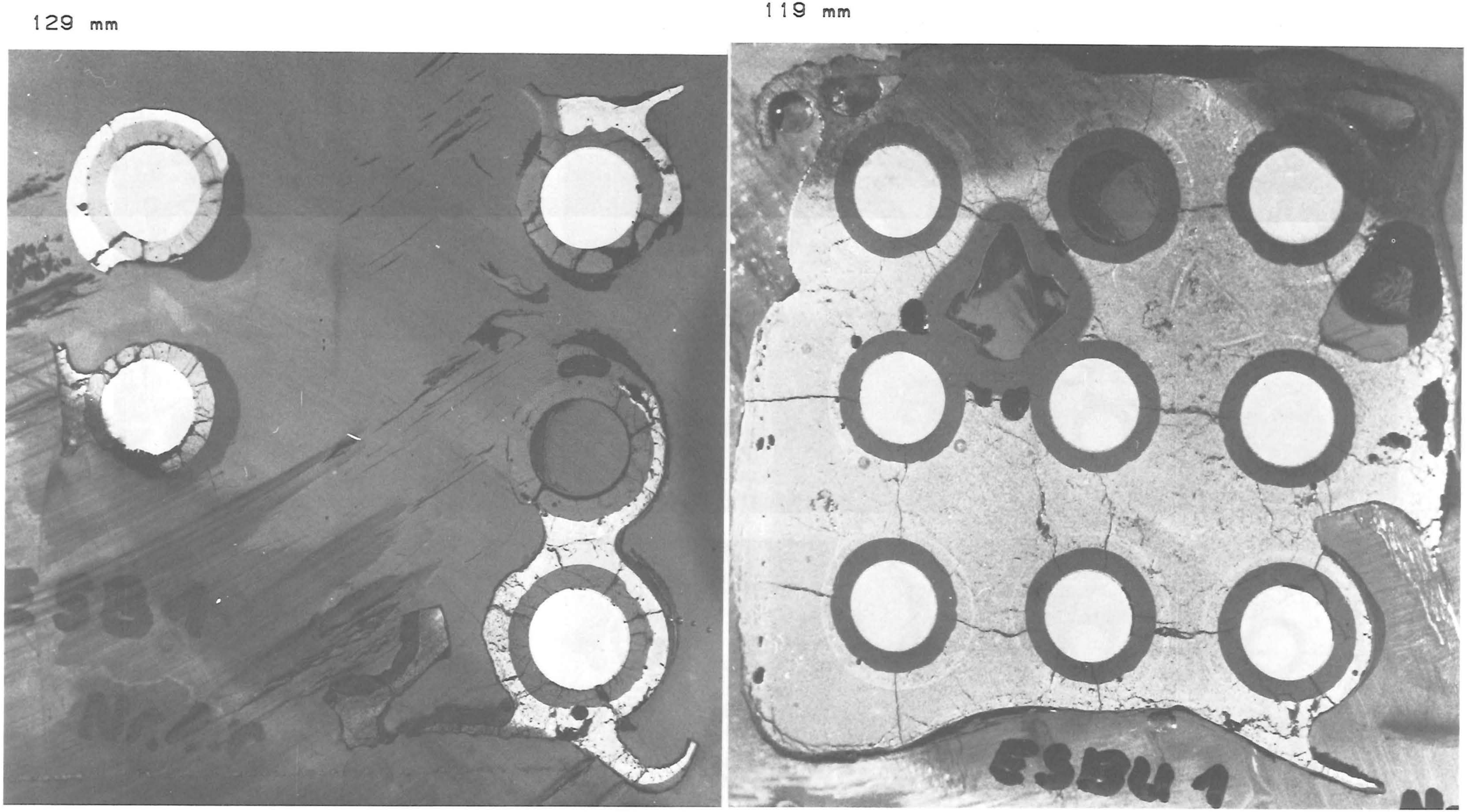
129 mm

119 mm

FIGURE 15: CROSS SECTIONS OF ESBU-1 AT 129 AND 119 MM ABOVE THE BOTTOM OF THE BUNDLE

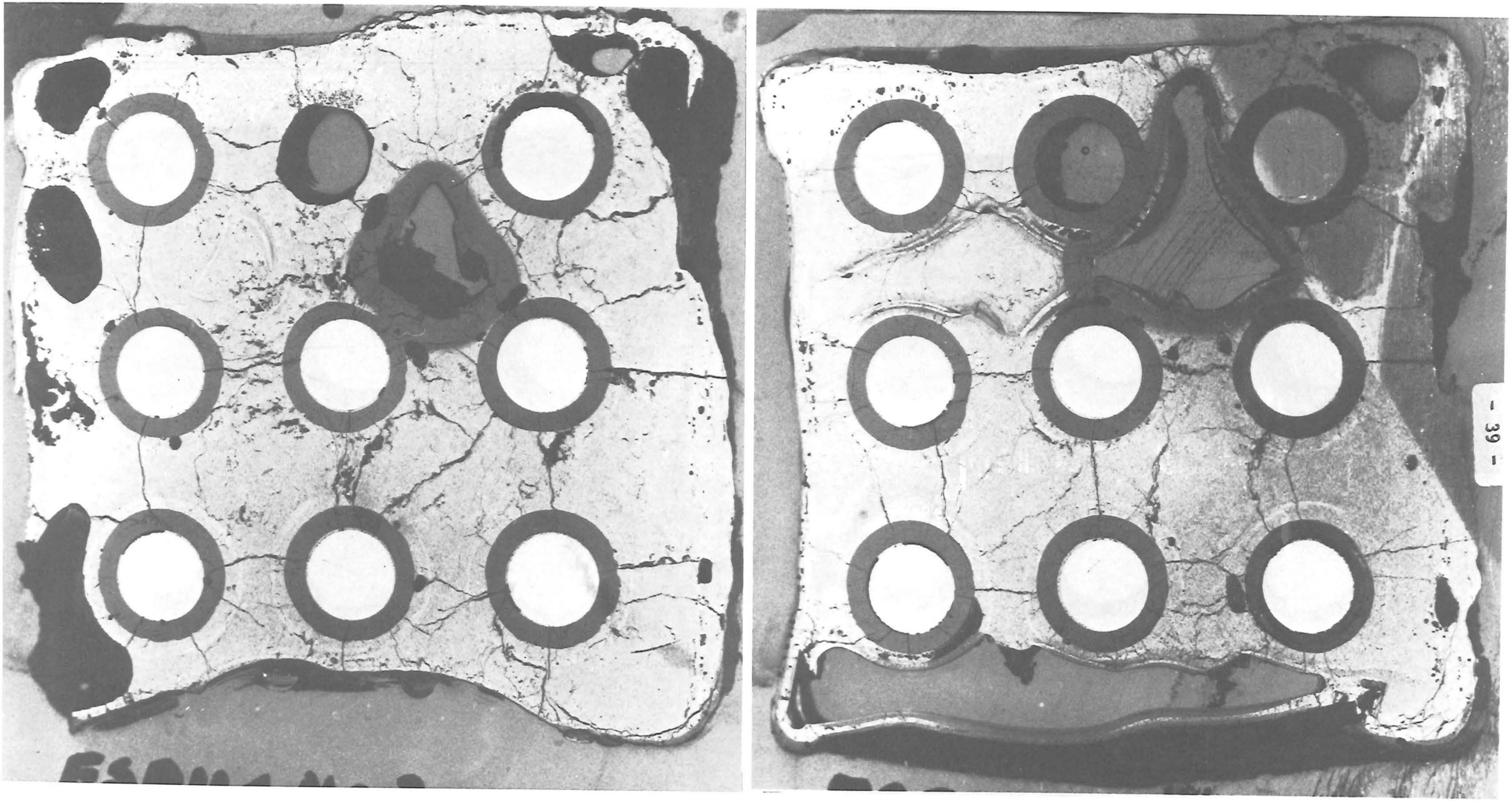

116 mm

106 mm

FIGURE 16: CROSS SECTIONS OF ESBU-1 AT 116 AND 106 MM ABOVE THE BOTTOM OF THE BUNDLE

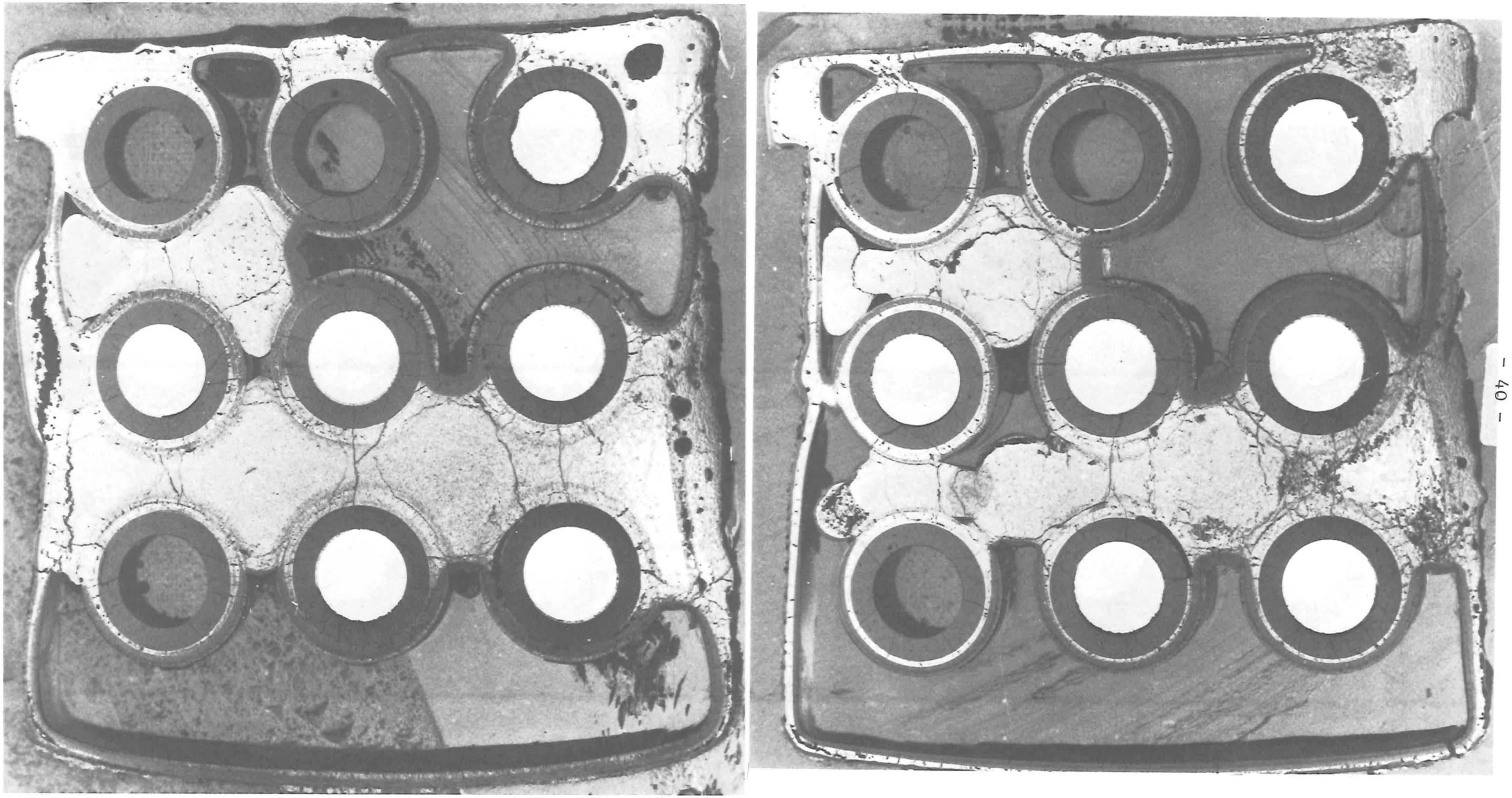

96 mm

86 mm

FIGURE 17: CROSS SECTIONS OF ESBU-1 AT 96 AND 86 MM ABOVE THE BOTTOM OF THE BUNDLE

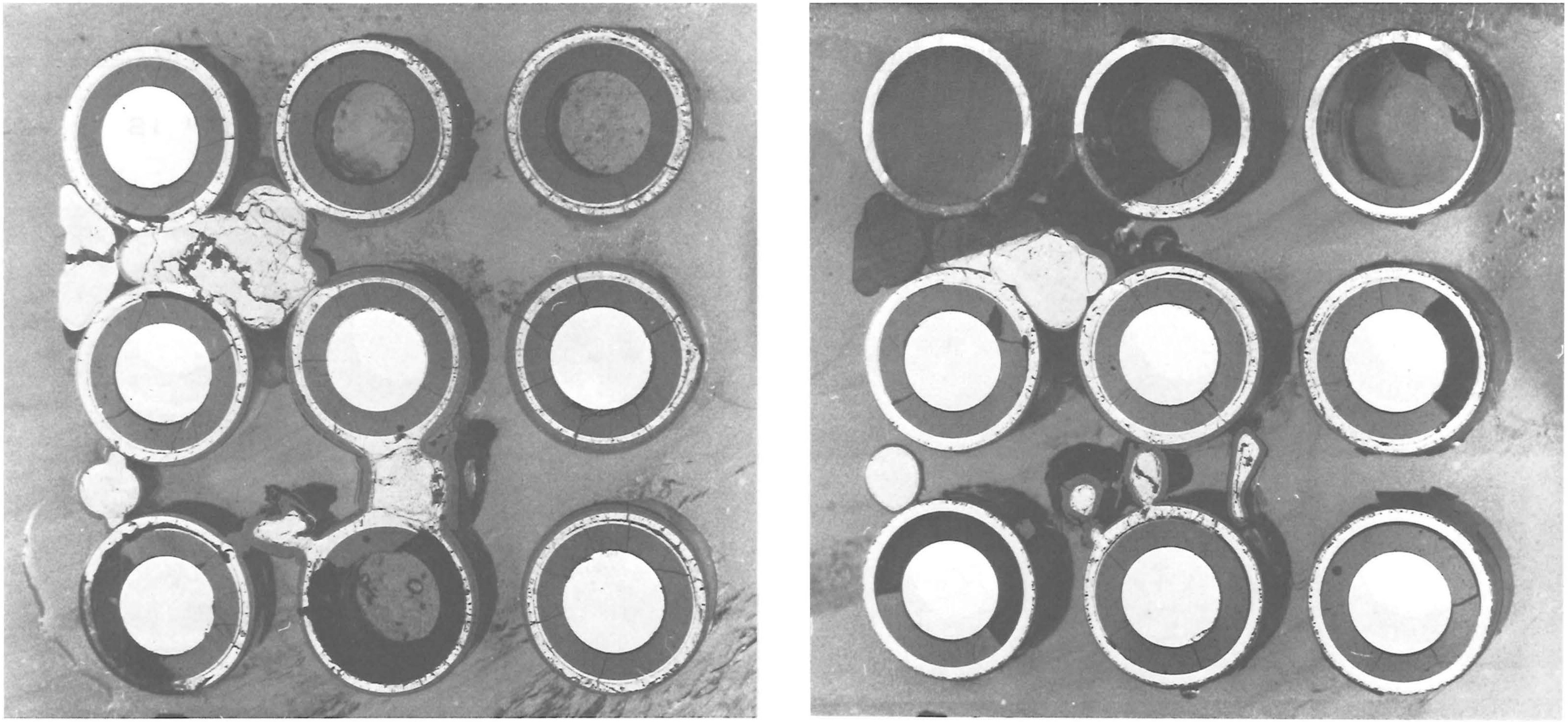

76 mm

66 mm

FIGURE 18: CROSS SECTIONS OF ESBU-1 AT 76 AND 66 MM ABOVE THE BOTTOM OF THE BUNDLE

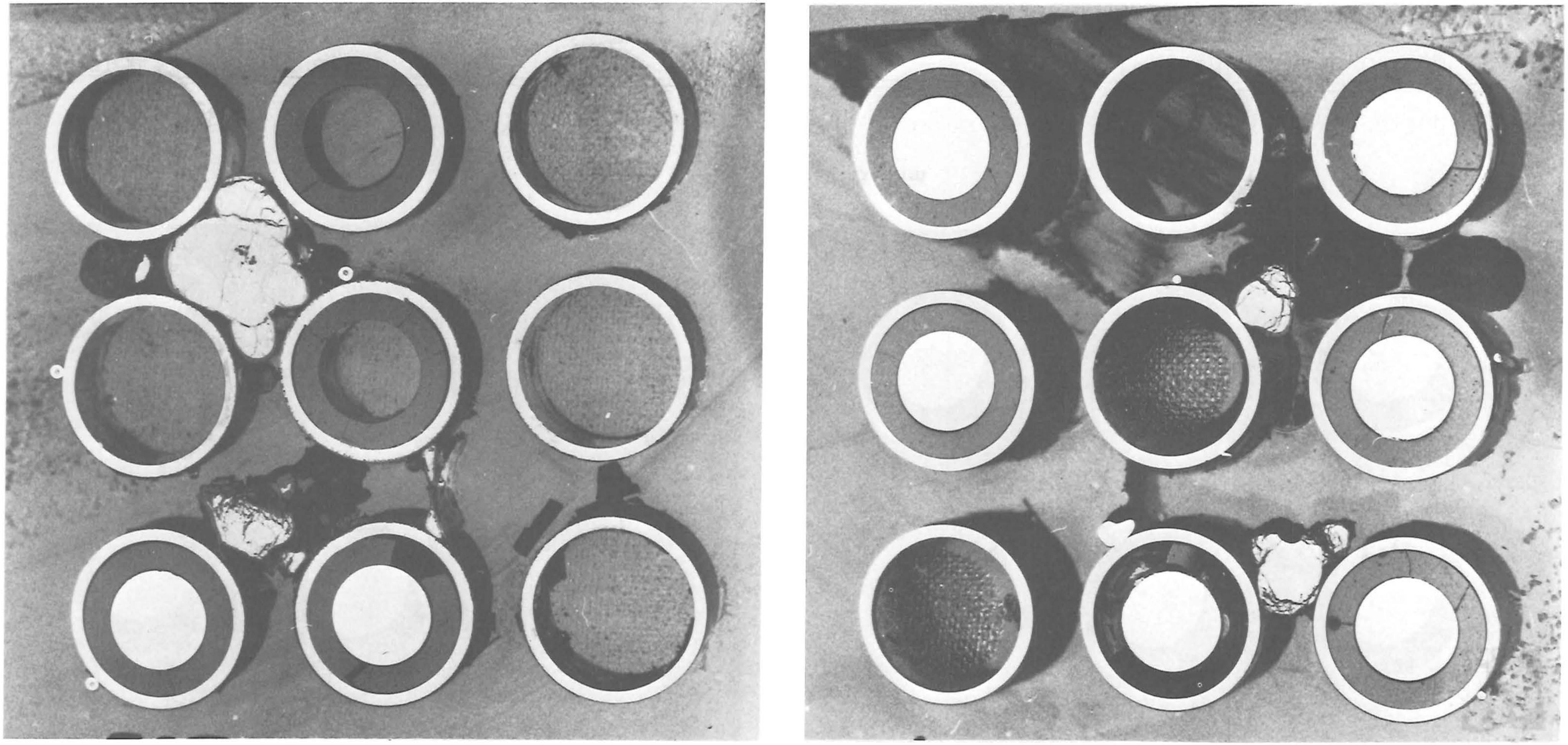

51 mm

15 mm

FIGURE 19: CROSS SECTIONS OF ESBU-1 AT 51 AND 15 MM ABOVE THE BOTTOM OF THE BUNDLE

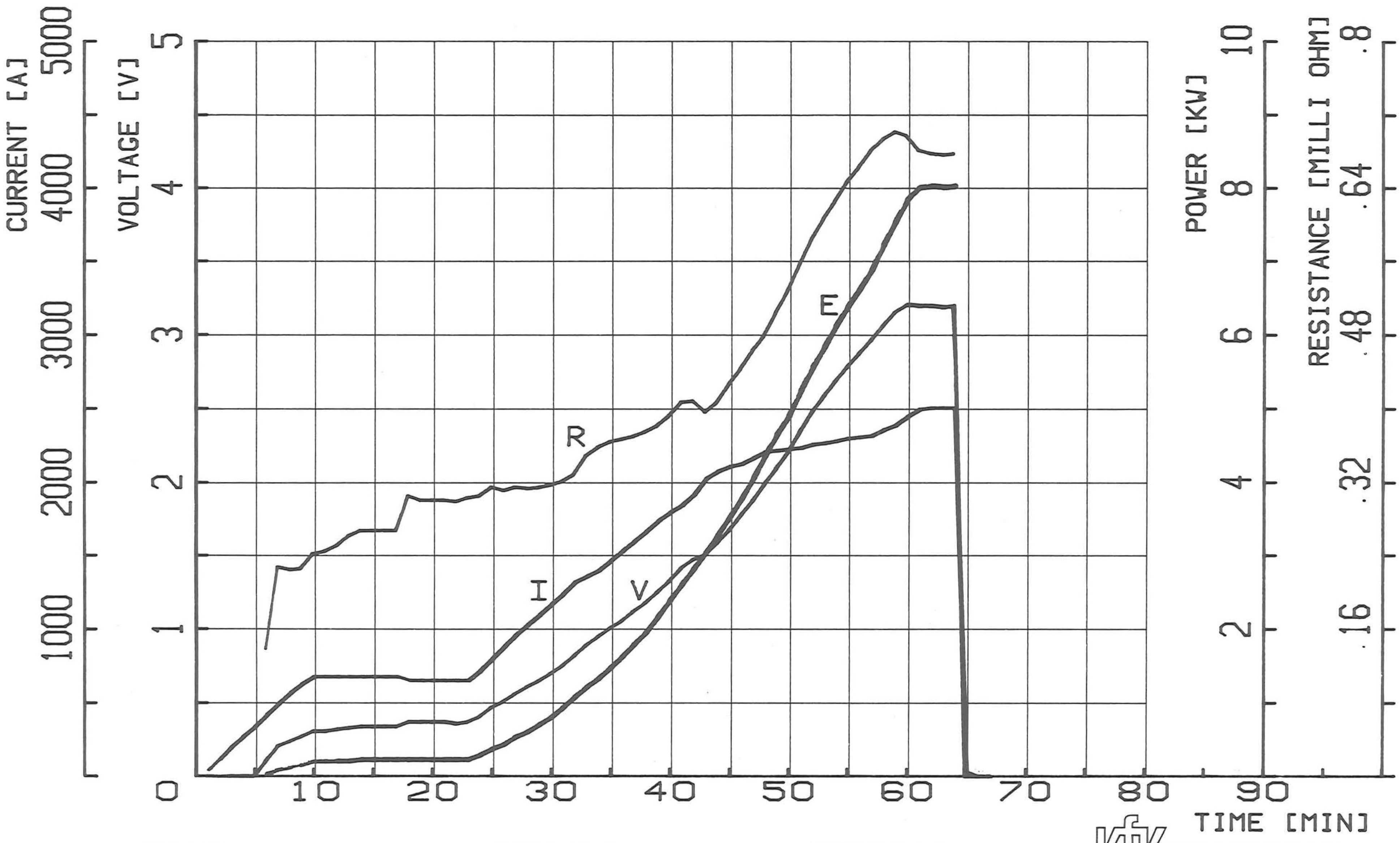

HAGEN ET AL. KFK-REPORT 3508

FIG.20: VOLTAGE V, CURRENT I, ELECTRIC POWER E AND RESISTANCE R FOR TEST ESBU-1

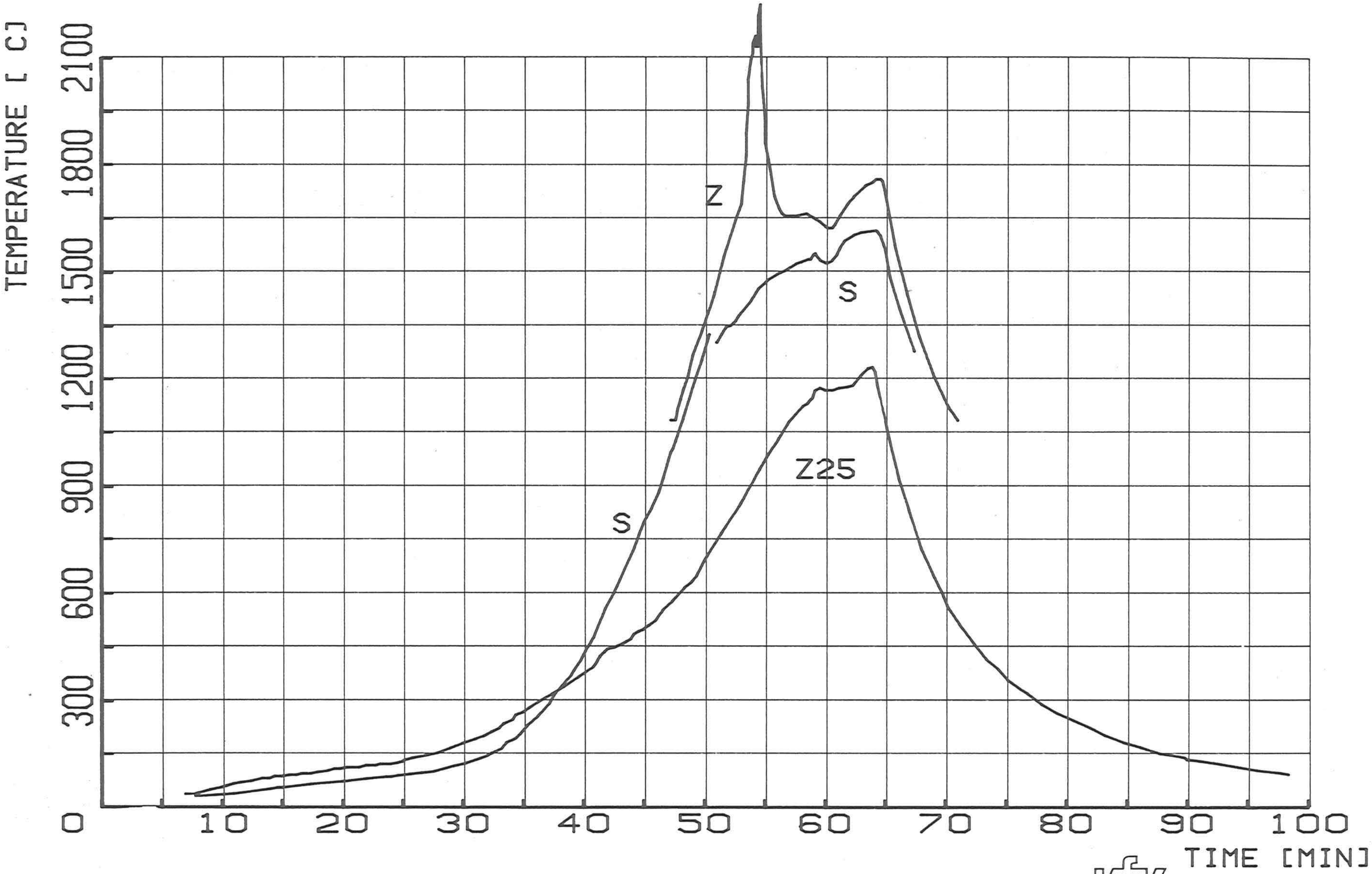

PNS KfK IT

FIG.21A: TEMPERATURES ON THE CENTRAL ROD (Z) AND SHROUD (S) AT 145 MM AND TEMPERATURE ON THE CENTRAL ROD AT 25 MM (Z25) FROM THE UPPER END OF THE CLADDING. ESBU-1

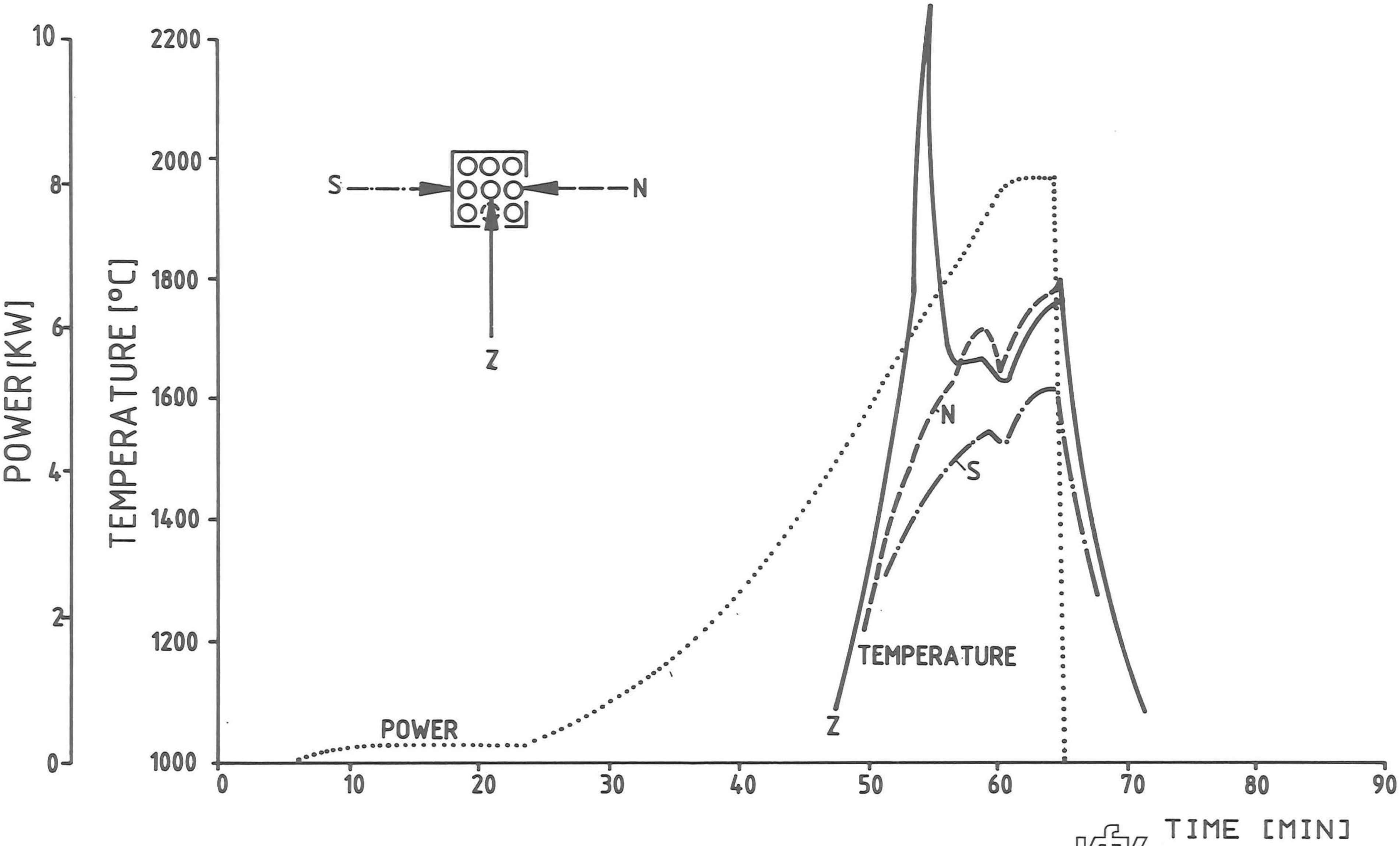

HAGEN ET AL. KFK-REPORT 3508

PNS KfK IT

FIG.21: TEMPERATURES ON THE CENTRAL ROD (Z), SIDE ROD (N) AND SHROUD (S) 145 MM FROM THE UPPER END OF CLADDING COMPARED TO THE ELECTRIC POWER INPUT FOR ESBU-1

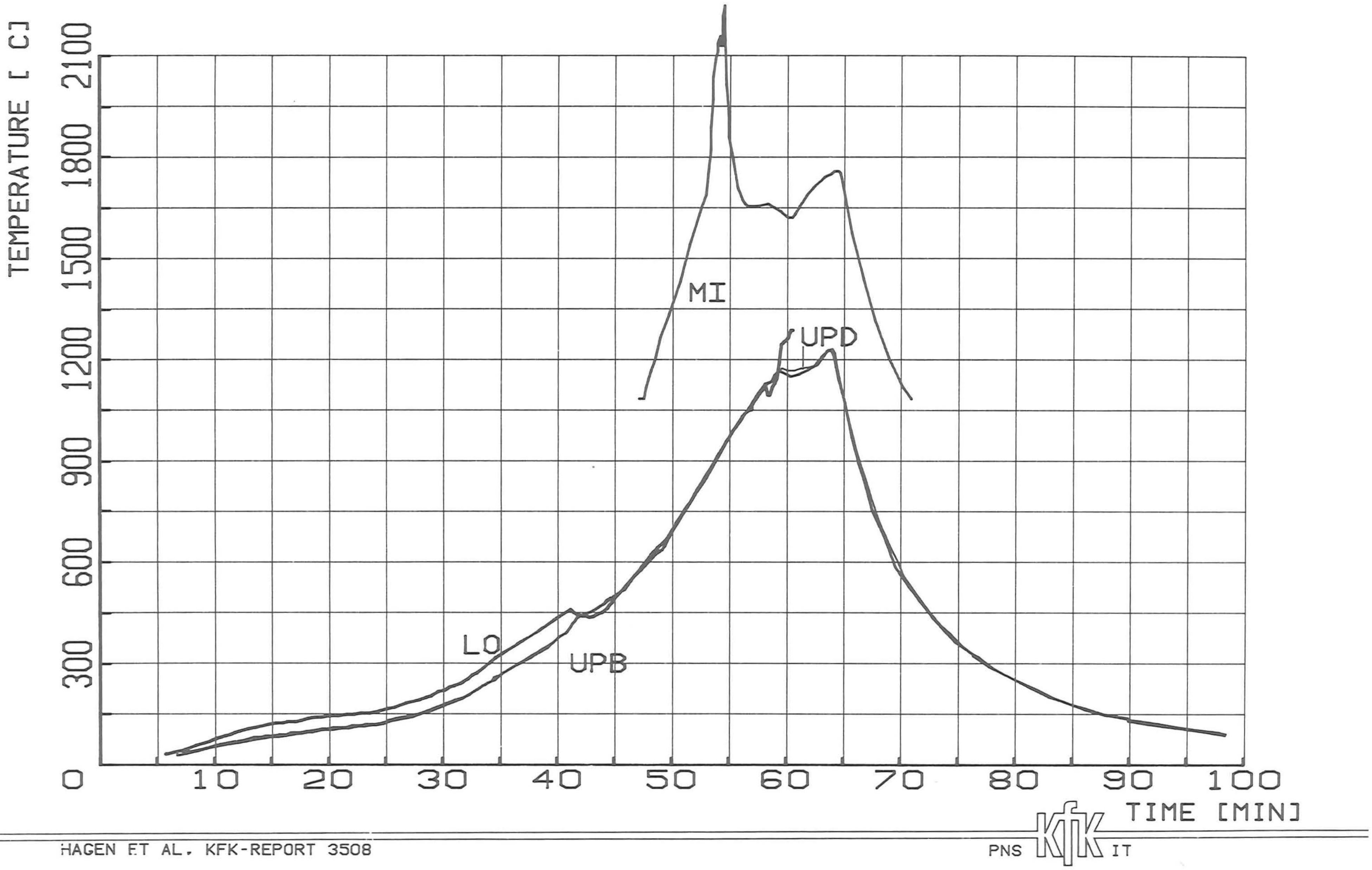

FIG. 22: TEMPERATURES ON THE CENTRAL ROD AT 50 MM FROM THE LOWER END (LO). AND 25 MM (UPB AND UPD) AND 145 MM (MI) FROM THE UPPER END : ESBU-1

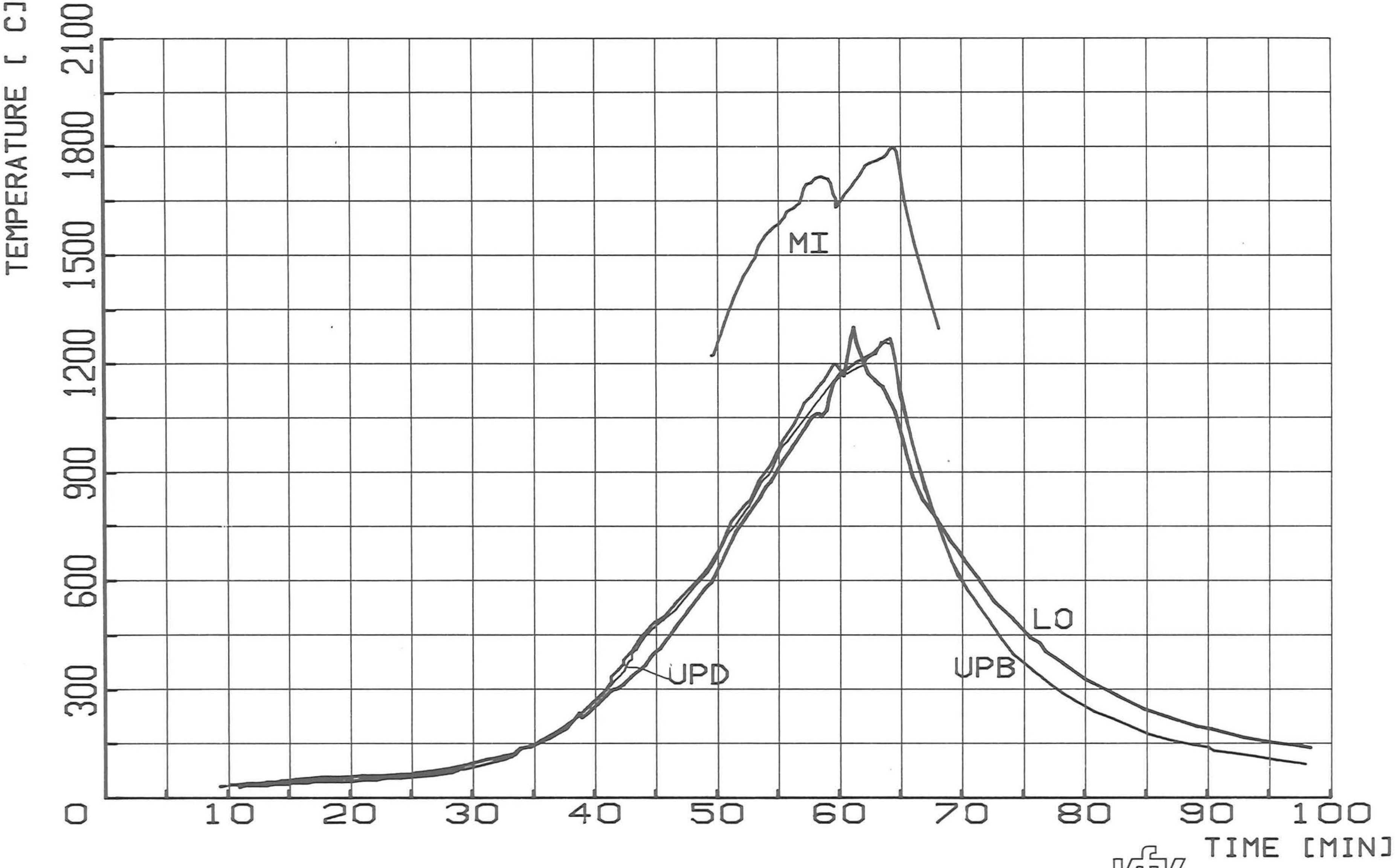

FIG.23: TEMPERATURES ON THE SIDE ROD AT 50 MM FROM THE LOWER END (LO), AND 25 MM (UPB AND UPD) AND 145 MM (MI) FROM THE UPPER END : ESBU-1

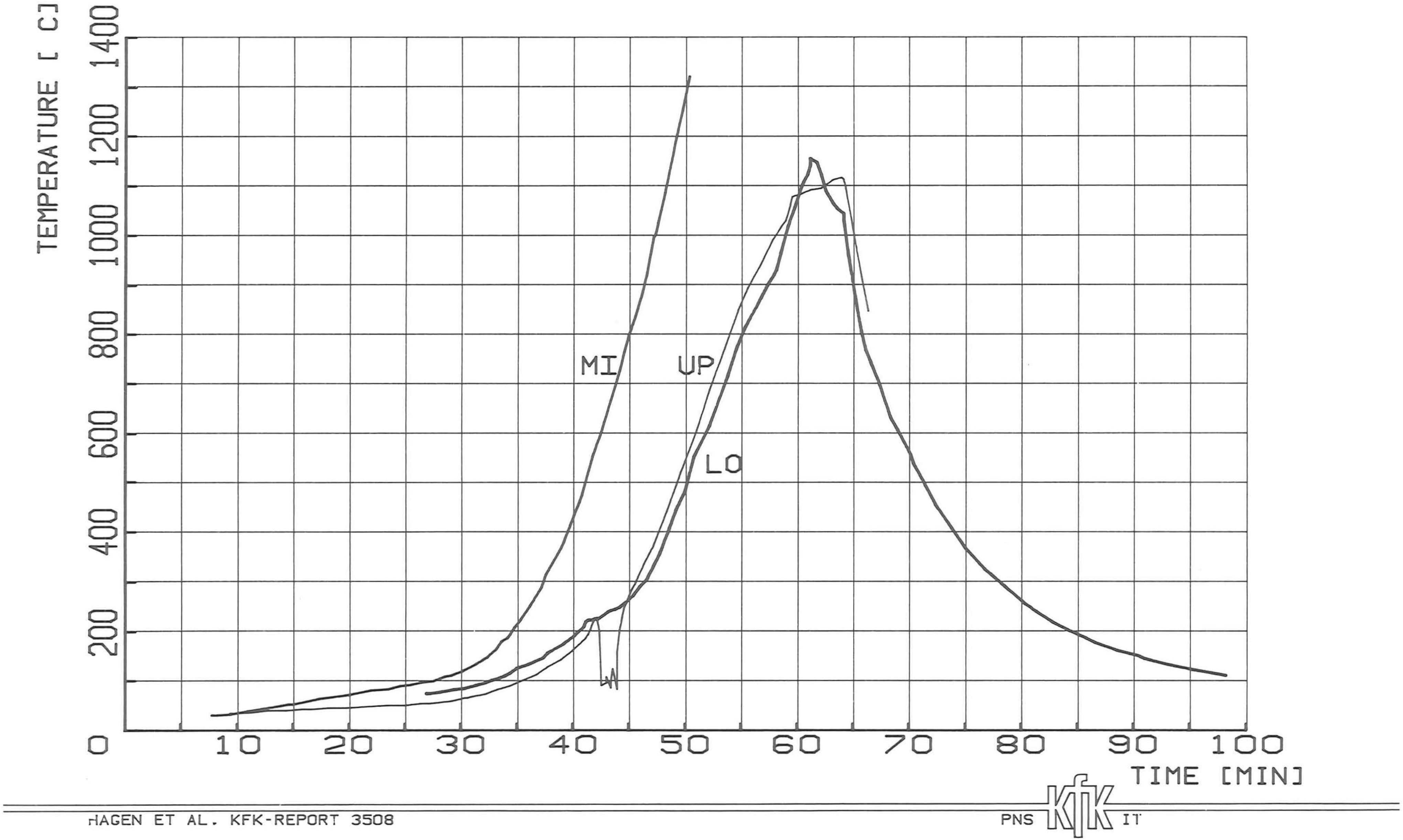

FIG.24: TEMPERATURES ON THE SHROUD AT 50 MM FROM THE LOWER END (LO). AND 25 MM (UP) AND 145 MM (MI) FROM THE UPPER END OF THE CLADDING : ESBU-1

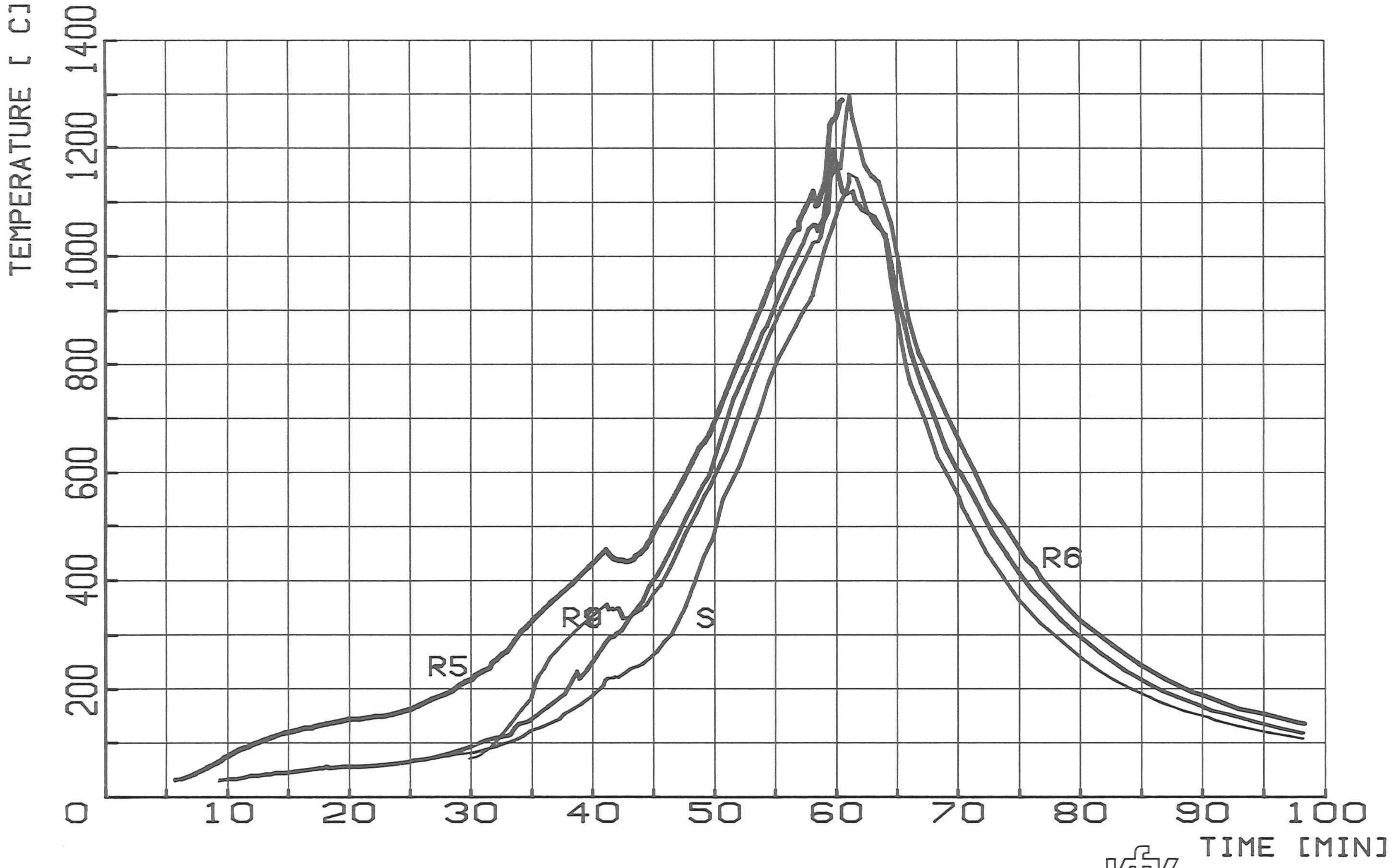

HAGEN ET AL. KFK-REPORT 3508

PNS KfK IT

FIG.25: TEMPERATURES ON THE CENTRAL ROD (R5). SIDE ROD (R6). CORNER ROD (R9) AND SHROUD (S) AT 50 MM FROM THE LOWER END OF THE CLADDING : ESBU-1

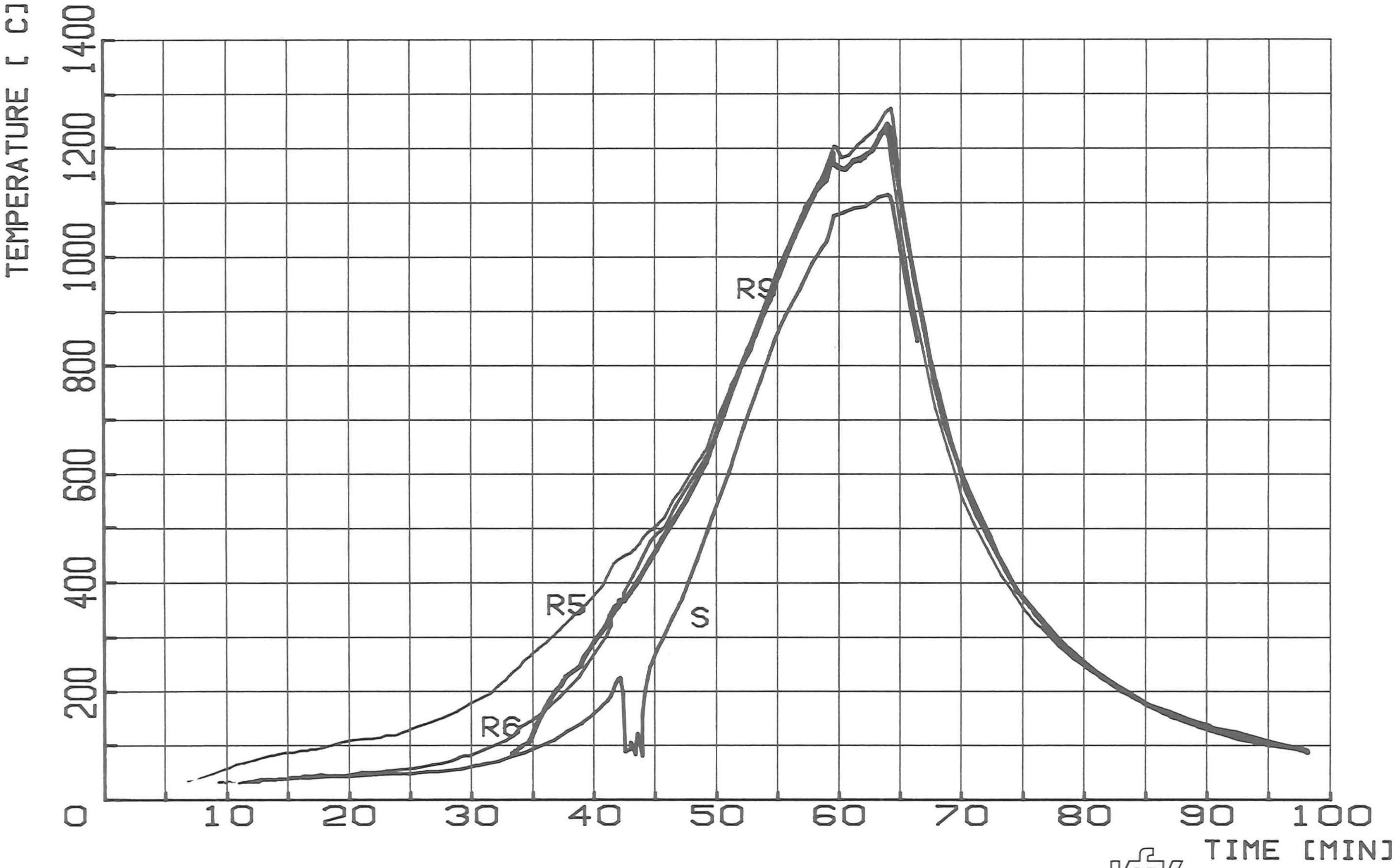

HAGEN ET AL. KFK-REPORT 3508

PNS KfK IT

FIG.26: TEMPERATURES ON THE CENTRAL ROD (R5).SIDE ROD (R6). CORNER ROD (R9) AND SHROUD (S) AT 25 MM FROM THE UPPER END OF THE CLADDING : ESBU-1

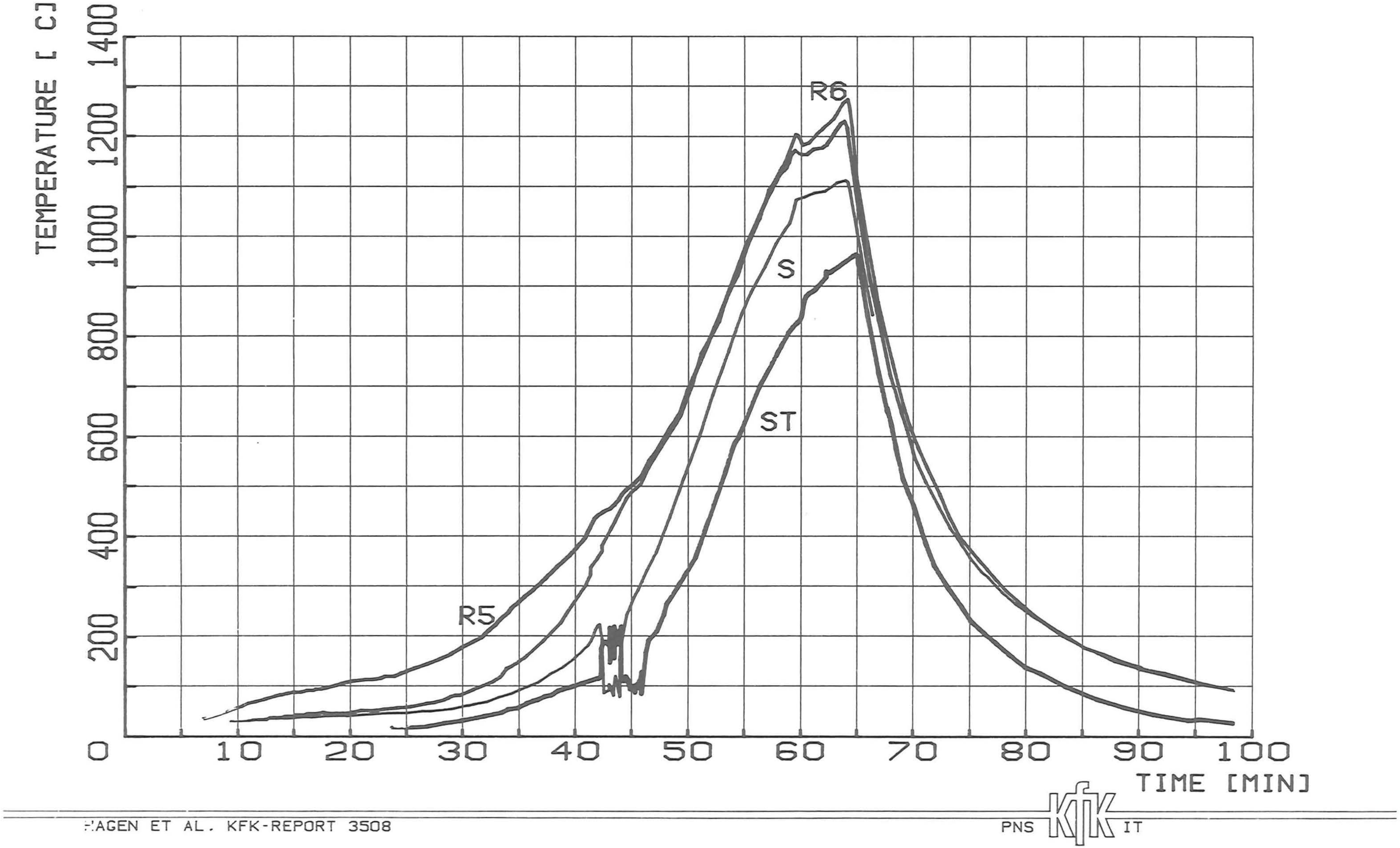

FIG.27: TEMPERATURES ON THE CENTRAL ROD (R5), SIDE ROD (R6) AND SHROUD (S) AT 25 MM FROM THE UPPER END IN COMPARISON TO THE STEAM TEMPERATURE (ST)

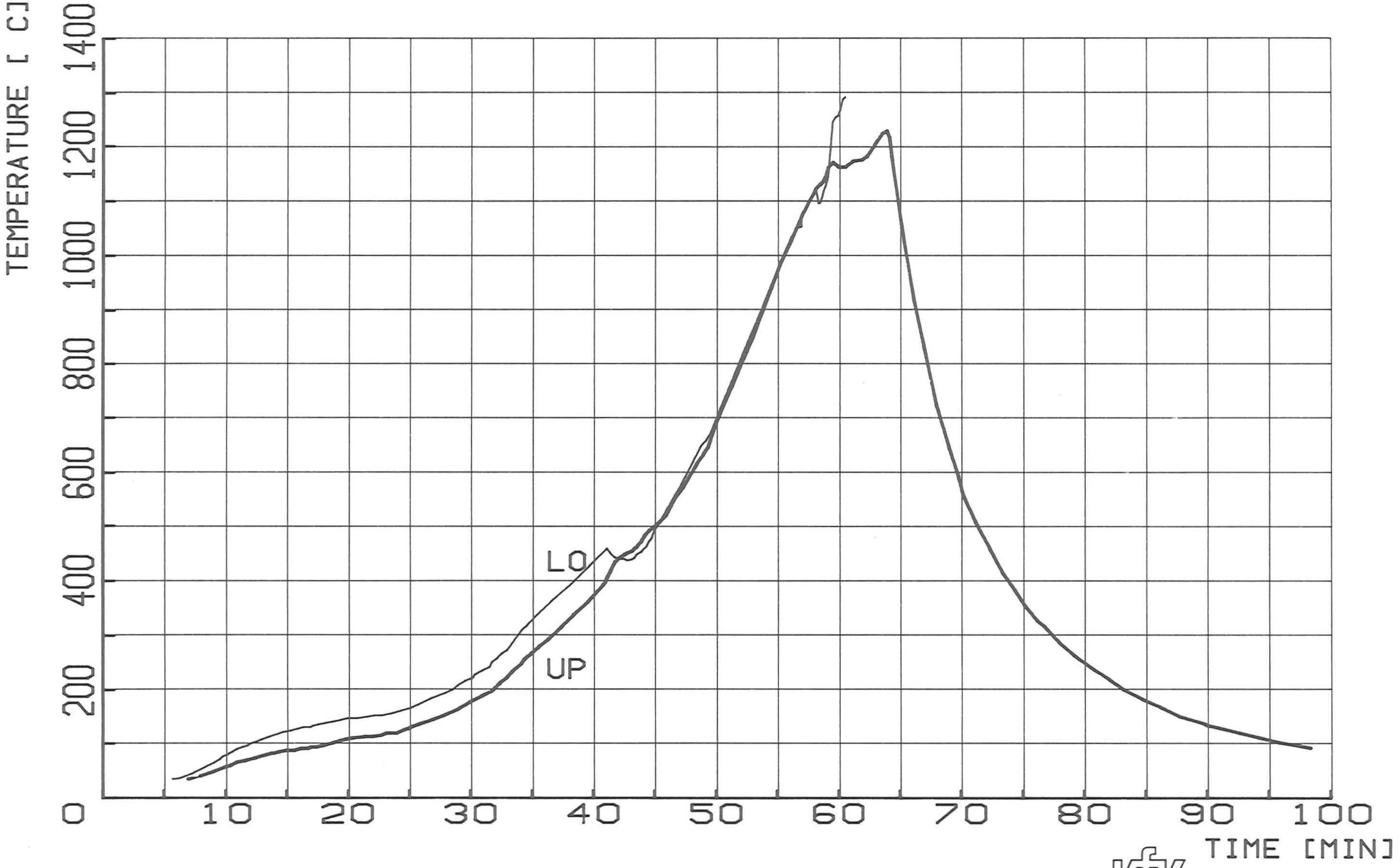

HAGEN ET AL. KFK-REPORT 3508 PNS KfK IT

FIG.28: TEMPERATURES ON THE CENTRAL ROD AT 50 MM FROM THE LOWER END (LO)
AND 25 MM FROM THE UPPER END (UP) OF THE CLADDING : ESBU-1

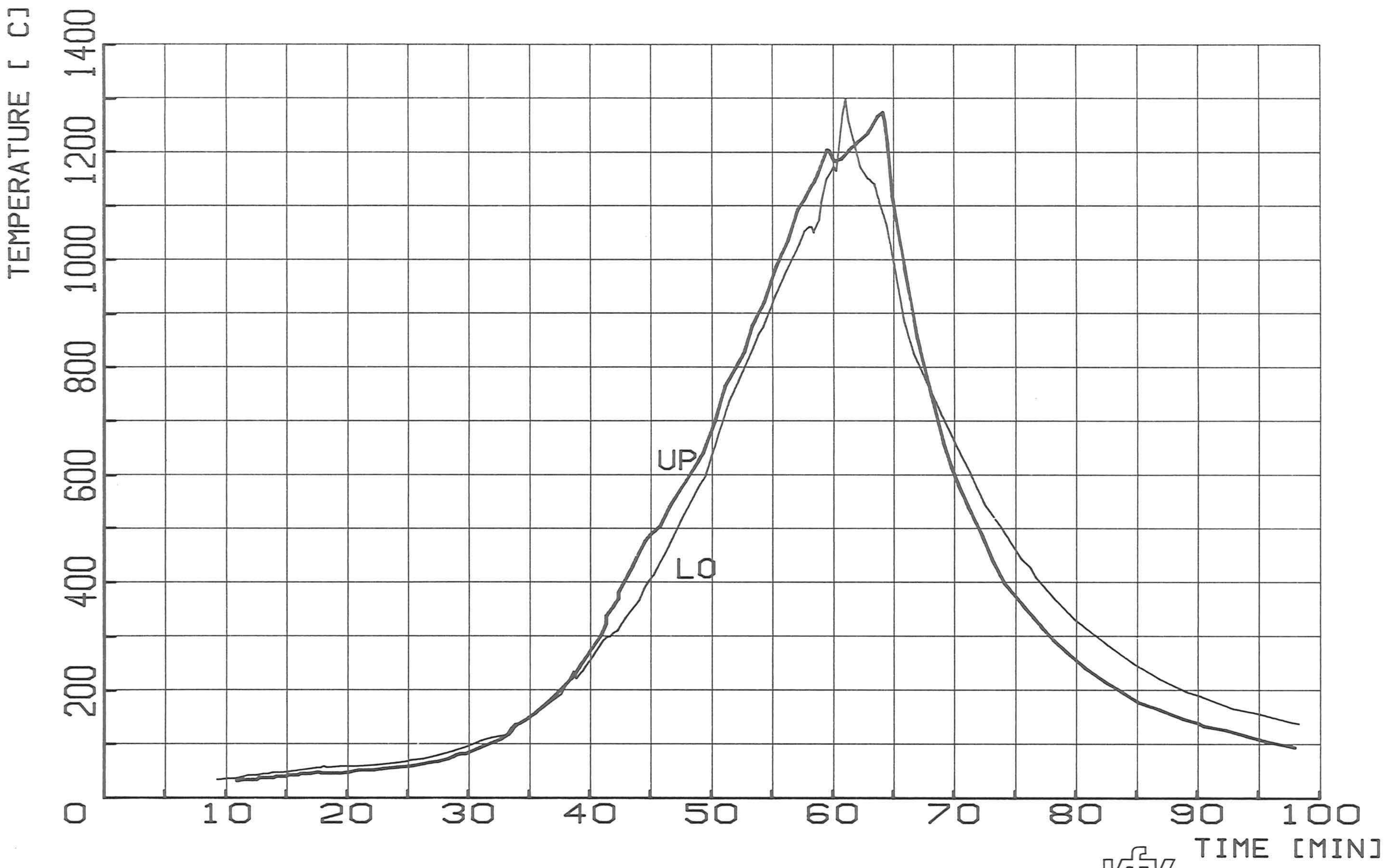

HAGEN ET AL. KFK-REPORT 3508 PNS KfK IT

FIG.29: TEMPERATURES ON A SIDE ROD (R6) AT 50 MM FROM THE LOWER END (LO) AND 25 MM FROM THE UPPER END (UP) OF THE CLADDING : ESBU-1

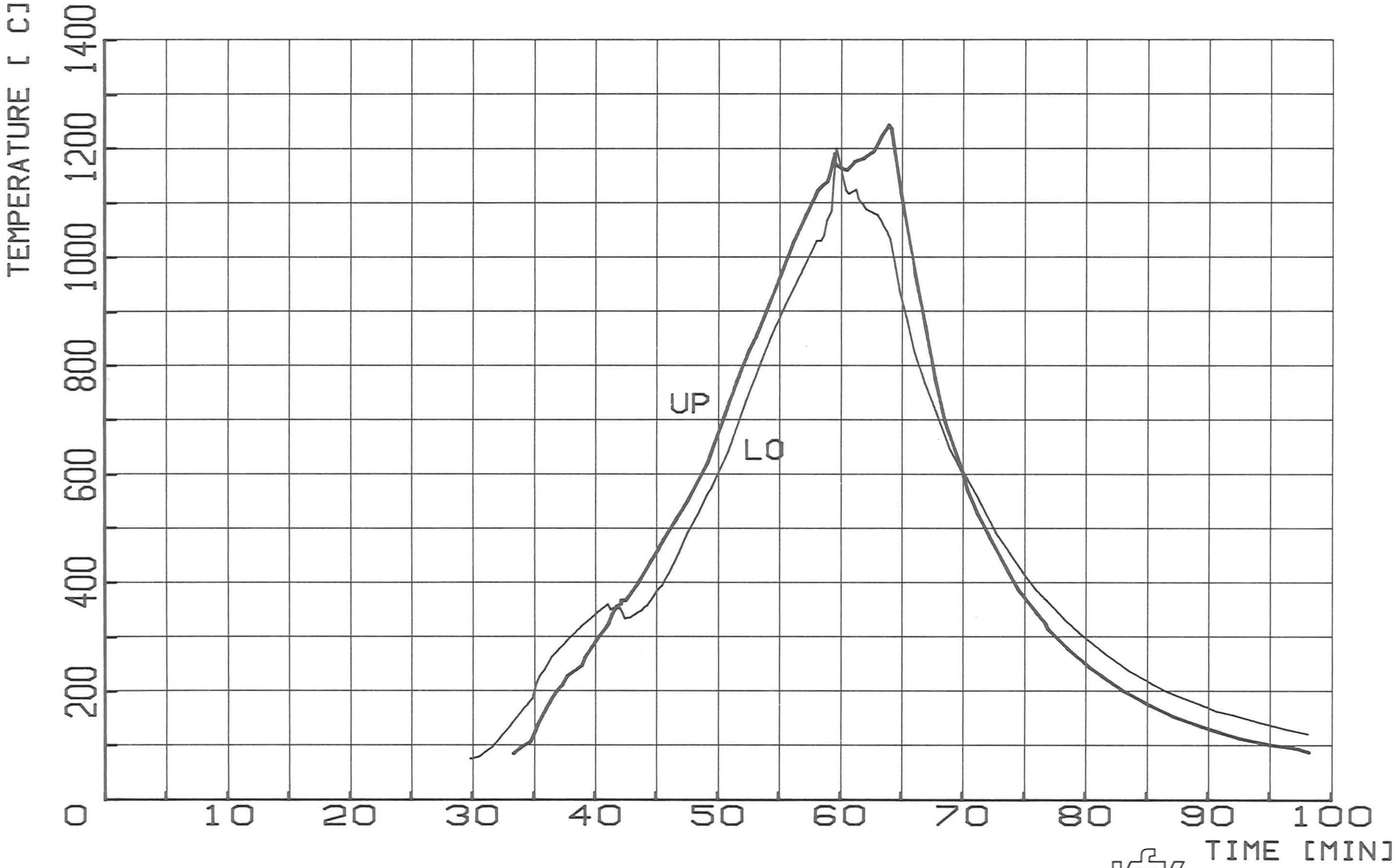

HAGEN ET AL. KFK-REPORT 3508 PNS KfK IT

FIG.30: TEMPERATURES ON A CORNER ROD (R9) AT 50 MM FROM THE LOWER END (LO) AND 25 MM FROM THE UPPER END (UP) OF THE CLADDING : ESBU-1

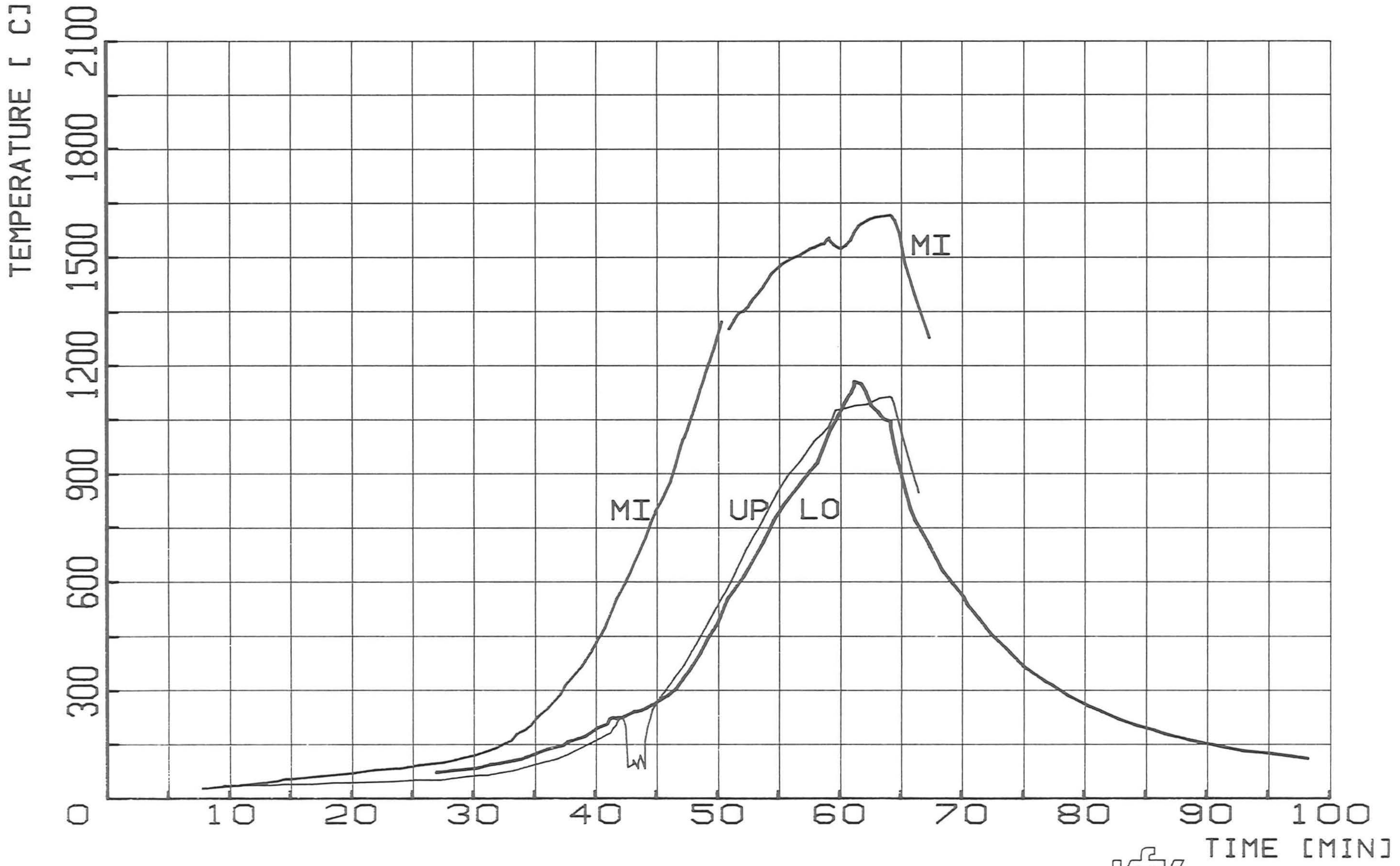

HAGEN ET AL. KFK-REPORT 3508

PNS KfK IT

FIG.31: TEMPERATURES ON THE SHROUD AT 50 MM FROM THE LOWER END (LO) AND 25 MM (UP) AND 145 MM (MI) FROM THE UPPER END OF THE CLADDING : ESBU-1

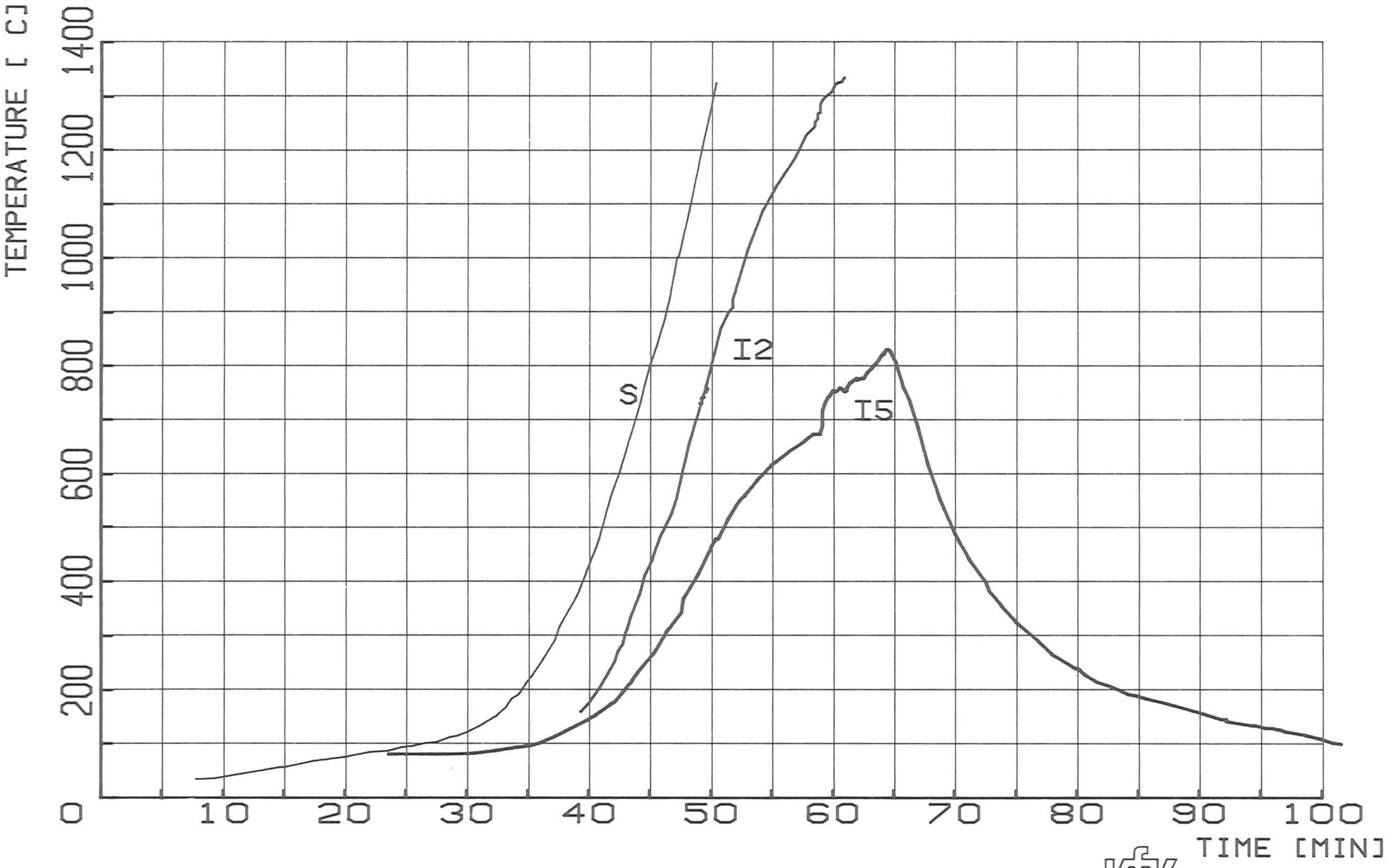

HAGEN ET AL. KFK-REPORT 3508 PNS KfK IT

FIG.32: TEMPERATURES AT 145 MM FROM THE UPPER END OF THE CLADDING ON THE SHROUD AT 2.5 MM (I2) AND 6.25 MM (I5) WITHIN THE FIBER CERAMIC INSULATION

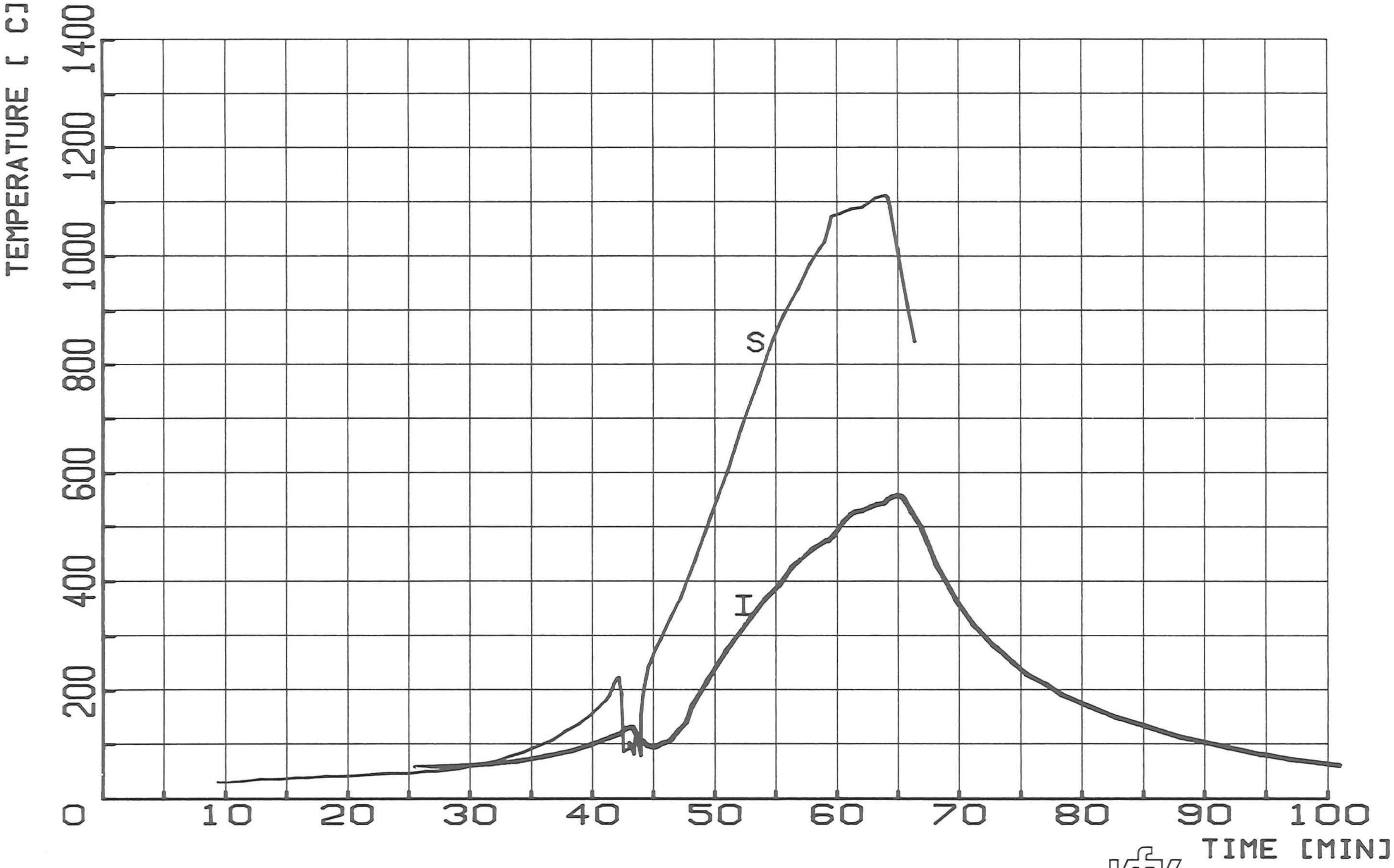

HAGEN ET AL. KFK-REPORT 3508

PNS KfK IT

FIG.33: TEMPERATURES ON THE SHROUD (S) AND ON THE SURFACE OF THE INSULATION (I)
AT 25 MM FROM THE UPPER END OF THE CLADDING : ESBU-1

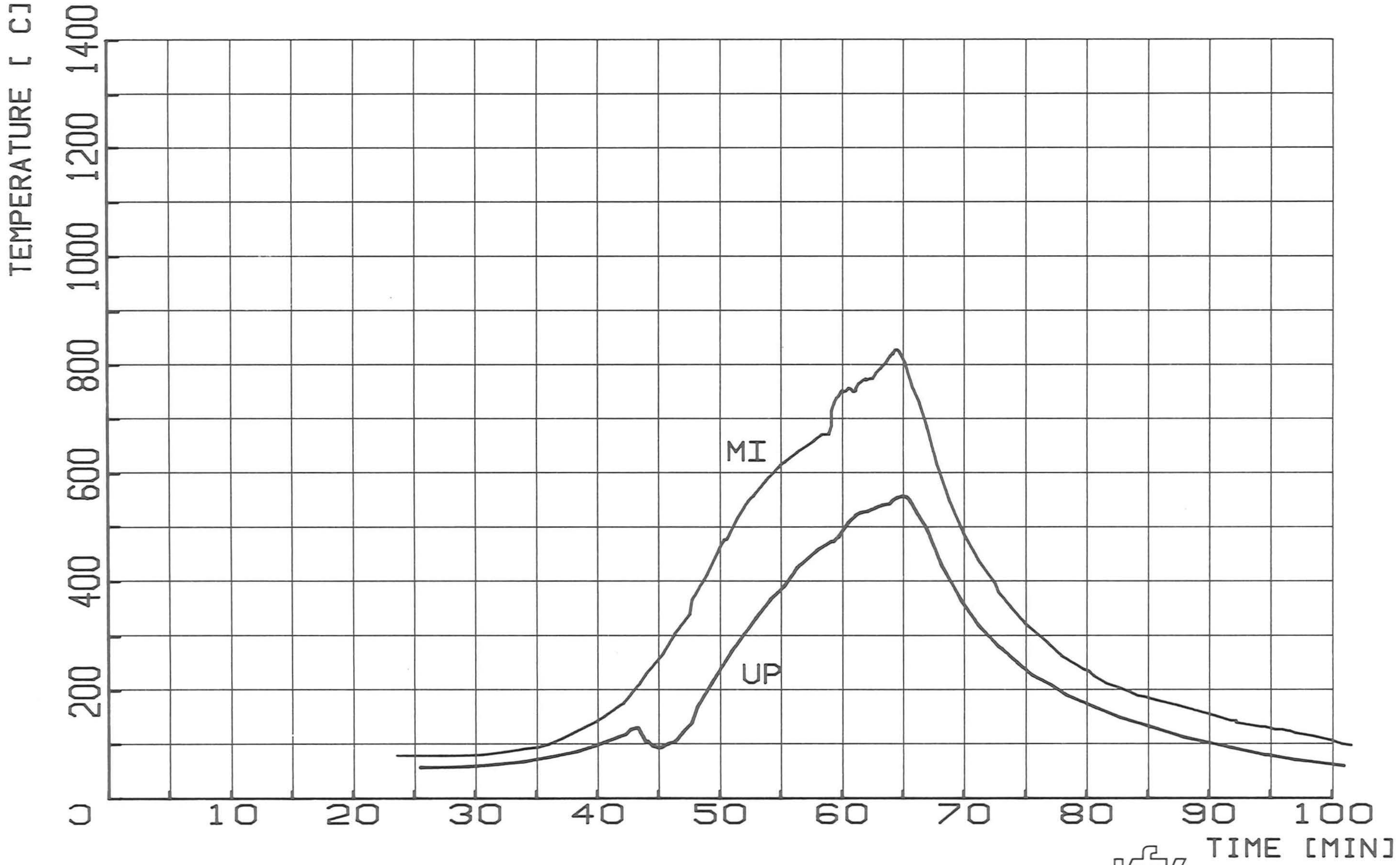

HAGEN ET AL. KFK-REPORT 3508

PNS KfK IT

FIG.34: TEMPERATURES ON THE SURFACE OF THE INSULATION AT 25 MM (UP)
AND 145 MM (MI) FROM THE UPPER END OF THE CLADDING : ESBU-1

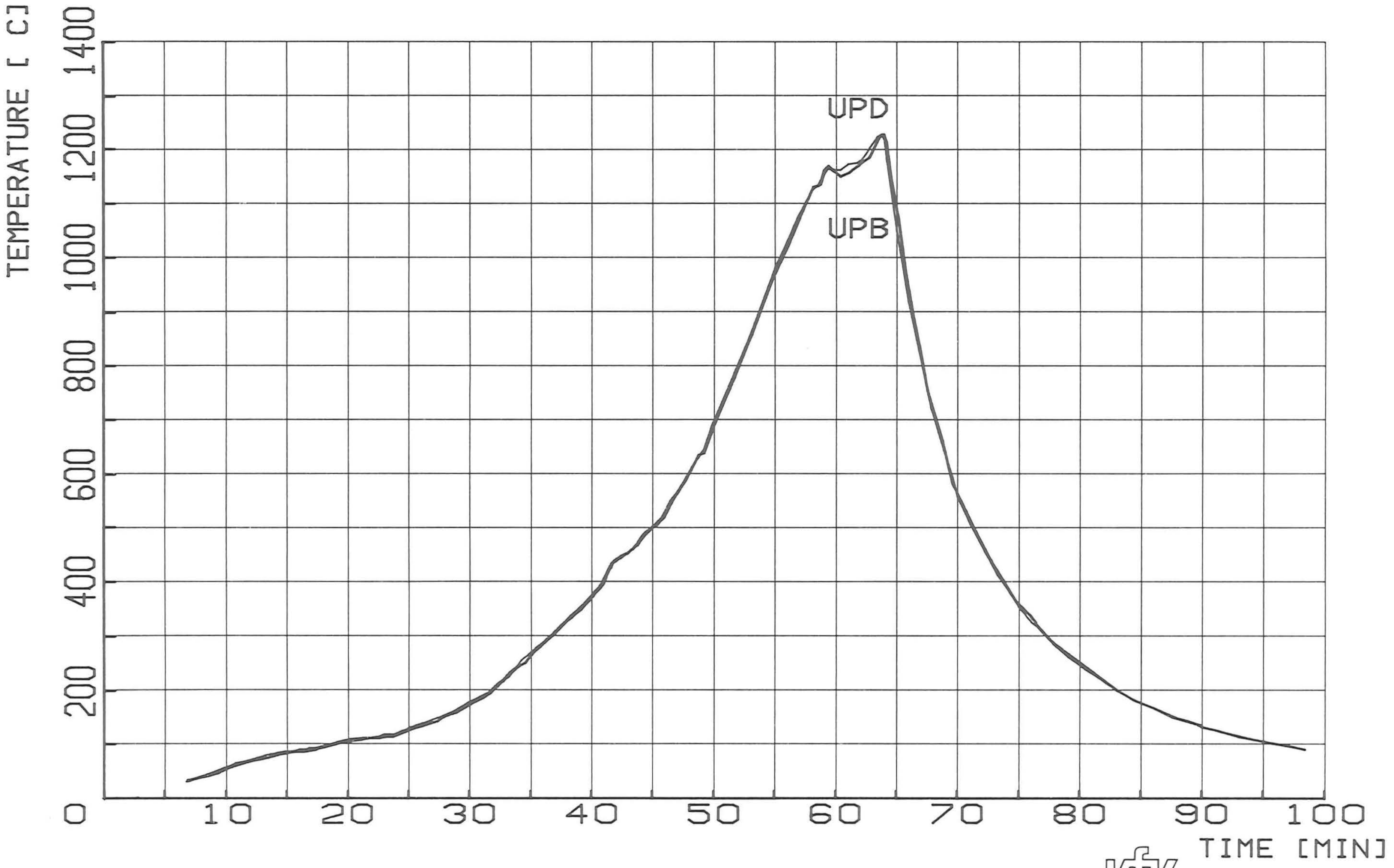

HAGEN ET AL. KFK-REPORT 3508 PNS KfK IT

FIG.35: TEMPERATURES ON TWO OPPOSITE SIDES (UPB AND UPD) OF THE CENTRAL ROD AT 25 MM FROM THE UPPER END OF THE CLADDING : ESBU-1

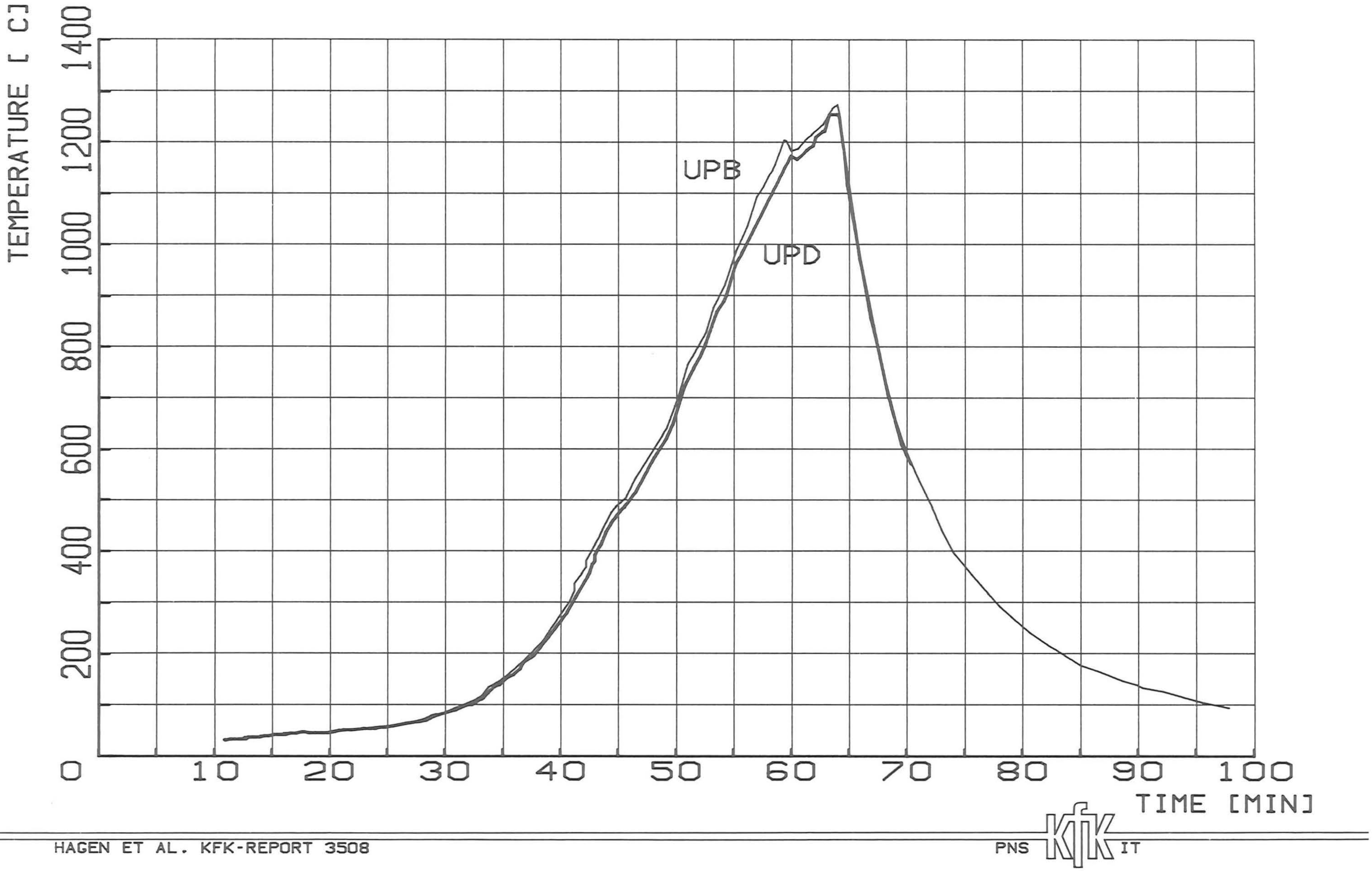

FIG.36: TEMPERATURES ON TWO OPPOSITE SIDES (UPB AND UPD) OF THE SIDE ROD (R6) AT 25 MM FROM THE UPPER END OF THE CLADDING : ESBU-1

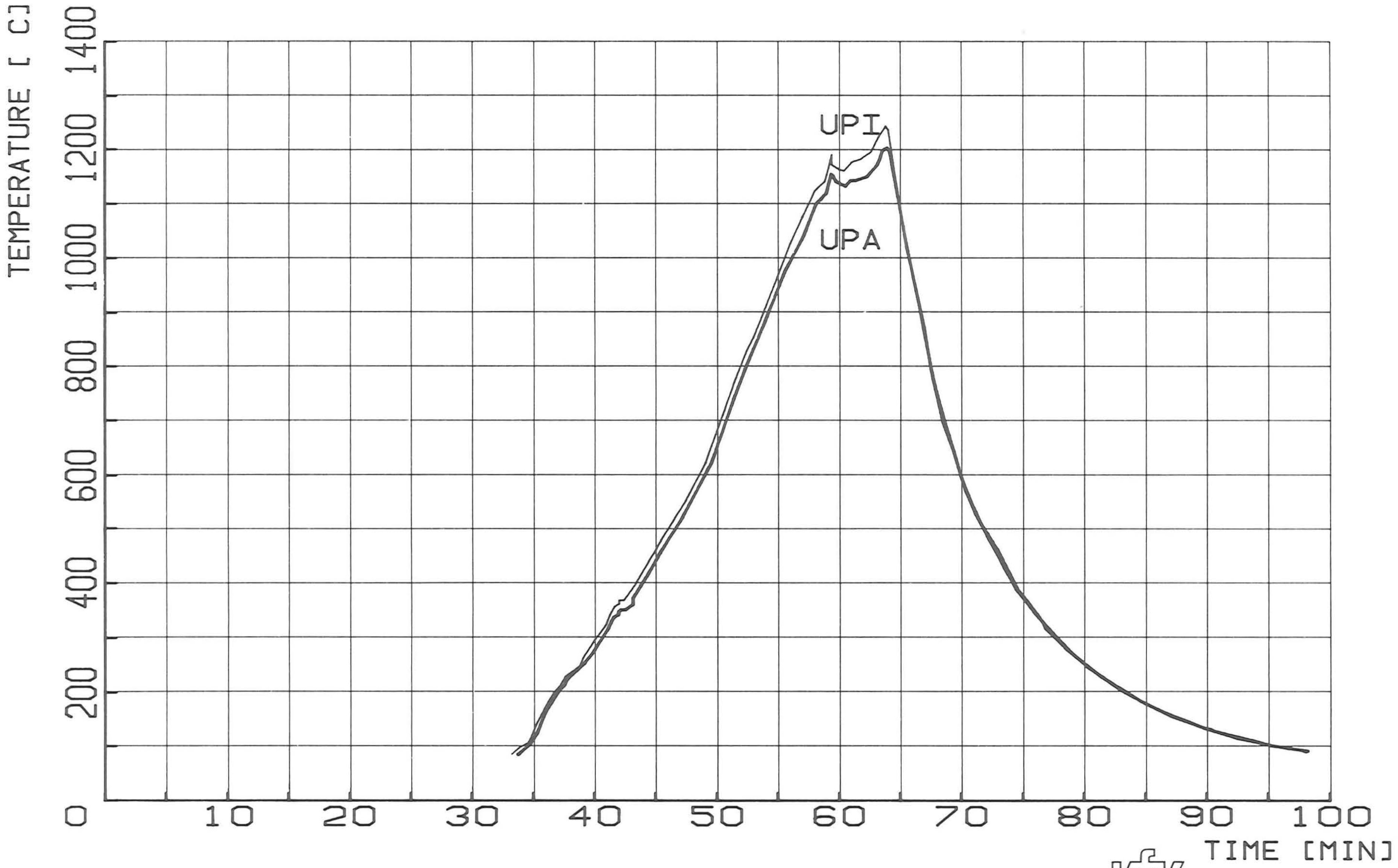

HAGEN ET AL. KFK-REPORT 3508 PNS KfK IT

FIG.37: TEMPERATURES ON TWO OPPOSITE SIDES (UPI AND UPA) OF A CORNER ROD (R9) AT 25 MM FROM UPPER END OF THE CLADDING : ESBU-1